



1

2       **Effects of transport on a biomass burning plume from Indochina**  
3                       **during EMERGe-Asia identified by WRF-Chem**

4

5       **Chuan-Yao Lin<sup>1\*</sup>, Wan-Chin Chen<sup>1</sup>, Yi-Yun Chien<sup>1</sup>, Charles C. K. Chou<sup>1</sup>, Chian-**  
6       **Yi Liu<sup>1</sup>, Helmut Ziereis<sup>2</sup>, Hans Schlager<sup>2</sup>, Eric Förster<sup>3</sup>, Florian Obsersteiner<sup>3</sup>,**  
7       **Ovid O. Krüger<sup>4</sup>, Bruna A. Holanda<sup>4</sup>, Mira L. Pöhlker<sup>4,a</sup>, Katharina Kaiser<sup>5,7</sup>,**  
8       **Johannes Schneider<sup>5</sup>, Birger Bohn<sup>8</sup>, Maria Dolores Andrés Hernández<sup>6</sup>, John P.**  
9       **Burrows<sup>6</sup>**

10

- 11       1. Research Center for Environmental Changes, Academia Sinica, Taipei, Taiwan  
12       2. Deutsches Zentrum für Luft- und Raumfahrt (DLR), Institut für Physik der  
13       Atmosphäre, Oberpfaffenhofen, Germany  
14       3. Karlsruhe Institute of Technology, Institute of Meteorology and Climate Research,  
15       Karlsruhe, Germany  
16       4. Multiphase Chemistry Department, Max Planck Institute for Chemistry, Mainz,  
17       Germany  
18       5. Particle Chemistry Department, Max Planck Institute for Chemistry, Mainz,  
19       Germany  
20       6. Institute of Environmental Physics, University Bremen, Bremen, Germany  
21       7. Institute for Atmospheric Physics, Johannes Gutenberg University, Mainz,  
22       Germany  
23       8. Institute of Energy and Climate Research IEK-8, Forschungszentrum Jülich, Jülich,  
24       Germany  
25       <sup>a</sup>now at: Faculty of Physics and Earth Sciences · Leipzig Institute for Meteorology,  
26       University of Leipzig/Experimental Aerosol and Cloud Microphysics Department,  
27       Leibniz Institute for Tropospheric Research, Leipzig, Germany

28

29

30       \*Corresponding author

31       **Chuan Yao Lin,**

32       Research Center for Environmental Changes, Academia Sinica, Taipei, Taiwan

33       128 Sec. 2, Academia Rd, Nankang, Taipei 115, Taiwan

34       (E-mail: [yao435@rceec.sinica.edu.tw](mailto:yao435@rceec.sinica.edu.tw), Tel.: +886-2-27875892, Fax: +886-2-27833584),

35       **Abstract.**



36 The Indochina biomass burning (BB) season in springtime has a substantial  
37 environmental impact on the surrounding areas in Asia. In this study, we evaluated the  
38 environmental impact of a major long-range BB transport event on 19 March 2018 (a  
39 flight of the HALO research aircraft, flight F0319) preceded by a minor event on 17  
40 March 2018 (flight F0317). Aircraft data obtained during the campaign in Asia of the  
41 Effect of Megacities on the transport and transformation of pollutants on the Regional  
42 to Global scales (EMeRGe) were available between 12 March and 7 April 2018. In the  
43 F0319, results of 1-min mean carbon monoxide (CO), ozone (O<sub>3</sub>), acetone (ACE),  
44 acetonitrile (ACN), organic aerosol (OA) and black carbon aerosol (BC) concentrations  
45 were up to 312.0 ppb, 79.0 ppb, 3.0 ppb, 0.6 ppb, 6.4 μg m<sup>-3</sup>, 2.5 μg m<sup>-3</sup> respectively,  
46 during the flight, which passed through the BB plume transport layer (BPTL) between  
47 the elevation of 2000–4000 m over the East China Sea (ECS). During F0319, CO, O<sub>3</sub>,  
48 ACE, ACN, OA and BC maximum of the 1 minute average concentrations were higher  
49 in the BPTL by 109.0 ppb, 8.0 ppb, 1.0 ppb, 0.3 ppb, 3.0 μg m<sup>-3</sup> and 1.3 μg m<sup>-3</sup>  
50 compared to flight F0317, respectively. Sulfate aerosol, rather than OA, showed the  
51 highest concentration at low altitudes (<1000 m) in both flights F0317 and F0319  
52 resulting from the continental outflow in the ECS.

53 The transport of BB aerosols from Indochina and its impacts on the downstream  
54 area was evaluated using a WRF-Chem model. Over the ECS, the simulated BB  
55 contribution demonstrated an increasing trend from the lowest values on 17 March 2018  
56 to the highest values on 18 and 19 March 2018 for CO, fine particulate matter (PM<sub>2.5</sub>),  
57 OA, BC, hydroxyl radicals (OH), nitrogen oxides (NO<sub>x</sub>), total reactive nitrogen (NO<sub>y</sub>),  
58 and O<sub>3</sub>; by contrast, the variation of J(O<sup>1</sup>D) decreased as the BB plume's contribution  
59 increased over the ECS. In the low boundary layer (<1000 m), the BB plume's  
60 contribution to most species in the remote downstream areas was <20 %. However, at  
61 the BPTL, the contribution of the long-range transported BB plume was as high as 30–



62 80 % for most of the species ( $\text{NO}_y$ ,  $\text{NO}_x$ ,  $\text{PM}_{2.5}$ , BC, OH,  $\text{O}_3$ , and CO) over South China  
63 (SC), Taiwan, and the ECS. BB aerosols were identified as a potential source of cloud  
64 condensation nuclei, and the simulation results indicated that the transported BB plume  
65 had an effect on cloud water formation over SC and the ECS on 19 March 2018. The  
66 combination of BB aerosol enhancement with cloud water resulted in a reduction of  
67 incoming shortwave radiation at the surface in SC and the ECS which potentially has  
68 significant regional climate implications.

69

70

## 71 **1 Introduction**

72 Biomass burning (BB) is one of the main sources of aerosols, greenhouse gases, and air  
73 pollutants (e.g. Ramanathan et al., 2007; Lin et al., 2009; 2014; Tang, 2003; Carmichael  
74 et al., 2003; Chi et al., 2010; Fu et al., 2012; Lin N.H. et al., 2012; Chuang et al., 2016).  
75 Reid et al. (2013) and Giglio et al. (2013) investigated the seasonal aerosol optical depth  
76 over Southeast Asia and have indicated that Indochina is a major contributor of carbon  
77 emissions in springtime. Galanter et al. (2000) estimated that BB accounts for 15–30 %  
78 of the entire tropospheric CO background. Huang et al. (2013) indicated that the  
79 contribution of BB in Southeast Asia to the aerosol optical depth (AOD) in Hong Kong  
80 and Taiwan could be in the range of 26–62 %. Moreover, BB emissions over Indochina  
81 are a significant contributor to black carbon (BC), organic carbon (OC), and  $\text{O}_3$  in East  
82 Asia (Lin et al., 2014). In their BB modeling study, Lin et al. (2014) identified a  
83 northeast (NE) to southwest (SW) zone stretching from South China (SC) to Taiwan  
84 with a reduction in shortwave radiation of approximately  $20 \text{ W m}^{-2}$  at the ground  
85 surface. In addition, the total carbon emission from BB in Southeast Asia is  
86 approximately  $91 \text{ Tg C yr}^{-1}$ , accounting for 4.9 % of the global total (Yadav et al.,  
87 2017). According to Xu et al. (2018), BB in Indochina leads to BC production at high



88 concentrations of up to  $2\text{--}6 \mu\text{g m}^{-3}$  in spring. The authors reported that BC particles  
89 were transported to the glaciers in the Tibetan Plateau, where it significantly affected  
90 the melting of the snow, causing some severe environmental problems, such as water  
91 resource depletion. Ding et al. (2021) indicated that BB aloft aerosols strongly increase  
92 the low cloud coverage over both land and ocean and affect the monsoon in the  
93 subtropical Southeast Asia.

94 Although many researchers have indicated the importance of BB emissions, their  
95 precise estimation and applying in the modeling study remains challenging (Fu et al.  
96 2012; Huang et al. 2013; Pimontree et al. 2018; Marvin et al. 2021). For example,  
97 Heald et al. (2003) conducted an emission inventory in Southeast Asia and reported that  
98 the uncertainties of BB emission estimations could be a factor of three or even higher.  
99 Following an inverse model analysis, Palmer et al. (2003) also indicated the  
100 overestimation of regional BB emissions over Indochina. Shi and Yamaguchi (2014)  
101 pointed out BB emissions exhibited similar temporal trends between 2001 and 2010  
102 and with strong interannual variability over southeast Asia. Satellite data can be used  
103 to easily locate hotspots such as those where agricultural residuals burning and forest  
104 wildfires are occurring worldwide. However, accurately quantifying the amount of BB  
105 emission from satellite data is difficult because anthropogenic pollutants and BB  
106 emissions are typically mixed in the atmosphere. During the NASA Transport and  
107 Chemical Evolution over the Pacific (TRACE-P) aircraft mission in spring 2001, Jacob  
108 et al. (2003) observed that warm conveyor belts (WCBs) lift both anthropogenic and  
109 BB (from SE Asia) air pollution to the free troposphere, resulting in complex chemical  
110 signatures. Wiedinmyer et al. (2011) demonstrated that the uncertainty of emission  
111 estimation could be as high as a factor of 2 because of the error introduced by estimates  
112 in fire hotspots, area burned, land cover maps, biomass consumption, and emission  
113 factors in the model. In this context, Lin et al. (2014) highlighted the uncertainty of



114 emission estimation in the first version of Fire Inventory from NCAR (Wiedinmyer et  
115 al., 2011).

116 The transport of BB pollution is strongly dependent on the atmospheric structure  
117 and weather conditions. Tang et al. (2003) noted that most BB aerosols, having their  
118 source in Indochina (mainly south of 25 °N and be alofted to an altitude of 2000–4000  
119 m) during the TRACE-P campaign were associated with outflow in the WCB region  
120 after frontal passage. Lin et al. (2009) suggested a mountain lee-side troughs as an  
121 important mechanism, resulting in BB product transport from the surface to >3000 m.  
122 BB pollution is often transported from its sources to the East China Sea (ECS), Taiwan,  
123 and the western North Pacific within a few days.

124 The airborne field experiment EMerGe ( Effect of Megacities on the transport and  
125 transformation of pollutants on the Regional to Global scales) over Asia was led by the  
126 University of Bremen, Germany and conducted in collaboration with Academia Sinica,  
127 during the inter-monsoon period in 2018 ([http://www.iup.uni-](http://www.iup.uni-bremen.de/emerge/home/home.html)  
128 [bremen.de/emerge/home/home.html](http://www.iup.uni-bremen.de/emerge/home/home.html)). The EMerGe aircraft mission consists of two  
129 parts. The first mission phase was conducted in Germany in July 2017 and the second  
130 phase was conducted from Taiwan in 2018 (Andrés Hernández et al. 2022). EMerGe in  
131 Asia aimed at the investigation of the long range transport (LRT) of local and regional  
132 pollution originating in Asian major population centers (MPCs) from the Asian  
133 continent into the Pacific. A central part of the project was the airborne measurement  
134 of pollution plumes on-board of the High Altitude and Long Range Research Aircraft  
135 (HALO). The HALO platform was based in Tainan, Taiwan (Fig. 1a-b), and made  
136 optimized transects and vertical profiling in regions north or south of Taiwan,  
137 dependent on the relevant weather and emission conditions. HALO measurements  
138 additionally provide important information for the evaluation of the LRT of BB  
139 emissions and its potential environmental impact in East Asia between 12 March and 7



140 April 2018. During the EMERGe-Asia campaign, HALO carried out 12 mission flights  
141 in Asia and 4 transfer flights from Europe to Asia with a total of 110 flight hours.

142 This paper is organized as follows: the model configuration and BB emission  
143 analysis employed in the model simulation are described in Section 2, and the weather  
144 conditions and HALO measurement results are presented in Section 3. The model  
145 performance, as well as the evaluation of BB product transport and effects on East Asia  
146 selected regions are discussed in Sections 4 and 5, respectively.

147

## 148 **2 Aircraft data and Model configuration**

### 149 **2.1 HALO aircraft data**

150 The HALO aircraft was equipped with a number of instruments and a detailed  
151 description of the measurement systems onboard the HALO was presented in Andrés  
152 Hernández et al.(2022). In this study, aerosol data (OA, BC,  $\text{SO}_4^{2-}$ ,  $\text{NO}_3^-$ ,  $\text{NH}_4^+$ ), and  
153 trace gases such as CO,  $\text{SO}_2$ ,  $\text{O}_3$ ,  $\text{NO}_x$ ,  $\text{NO}_y$ , acetone (ACE), acetonitrile (ACN), HCHO,  
154 HONO, OH,  $\text{HO}_2$ , and photolysis rate  $J(\text{O}^1\text{D})$ ,  $J(\text{NO}_2)$  were employed in the analysis.

### 155 **2.2 WRF-Chem Model and model configuration**

156 We used the Weather Research Forecasting with Chemistry (WRF-Chem) model (Ver.  
157 4.1.1) (Grell et al., 2005) to study the LRT of air masses associated with BB pollutants  
158 in Indochina. The initial and boundary meteorological conditions for WRF-Chem were  
159 obtained from National Centers for Environmental Prediction (NCEP)-GDAS Global  
160 Analysis data sets at 6-h intervals. The Mellor–Yamada–Janjic planetary boundary  
161 layer scheme (Janjic, 1994) was applied. The horizontal resolution for the simulations  
162 performed was 10 km, and the grid box had  $442 \times 391$  points in the east–west and  
163 north–south directions (Fig. 1a). A total of 41 vertical levels were included, with the  
164 lowest level at an elevation of approximately 50 m. To improve the accuracy of the  
165 meteorological fields, a grid nudging four-dimensional data assimilation scheme was



166 applied using the NCEP-GDAS Global Analysis data.

167 The cloud microphysics used followed the Lin scheme (Morrison et al., 2005). The  
168 rapid radiative transfer model (Zhao et al., 2011) was used for both longwave and  
169 shortwave radiation schemes. Moreover, land surface processes are simulated using the  
170 Noah-LSM scheme (Hong et al., 2009). In terms of transport processes, we considered  
171 advection by winds, convection by clouds, and diffusion by turbulent mixing. The  
172 removal processes in this study were gravitational settling, surface deposition, and wet  
173 deposition (scavenging in convective updrafts and rainout or washout in large-scale  
174 precipitation). The kinetic preprocessor (KPP) interface was used in both of the  
175 chemistry schemes of the Regional Atmospheric Chemistry Mechanism (RACM,  
176 Stockwell et al., 1990). The secondary organic aerosol formation module, the Modal  
177 Aerosol Dynamics Model for Europe (Ackermann et al., 1998)/Volatility Basis Set  
178 (Ahmadov et al., 2012), was also employed in the WRF-Chem model. In RACM, “KET”  
179 is the only species available for ketones. Thus, we do estimate the measurement of ACE  
180 by using simulated KET in this study.

181

### 182 **2.3 Emission Inventories**

183 Anthropogenic emissions, such as NO<sub>x</sub>, CO, SO<sub>2</sub>, nonmethane volatile organic  
184 compounds, sulfate, nitrate, PM<sub>10</sub>, and PM<sub>2.5</sub>, were adopted on the basis of the emission  
185 inventory in Asia – MICS-Asia III (Li et al., 2020; Kong et al., 2020). For BB emissions  
186 FINNv1.5 (<https://www.acom.ucar.edu/Data/fire/>) was employed. FINN provided  
187 daily, 1000 m resolution, global estimates of the trace gas and particle emissions from  
188 open BB, which included wildfires, agricultural fires, and prescribed burning but not  
189 biofuel use and trash burning (Wiedinmyer et al., 2011). The anthropogenic emissions  
190 in Taiwan were obtained from the Taiwan Emission Data System (TEDS) which is the  
191 emission inventory of the air-pollutant monitoring database of the Taiwan



192 Environmental Protection Administration. The TEDS version used for this study was  
193 V9.0 (2013) and contained data on eight primary atmospheric pollutants: CO, NO, NO<sub>2</sub>,  
194 NO<sub>x</sub>, O<sub>3</sub>, PM<sub>10</sub>, PM<sub>2.5</sub>, and SO<sub>2</sub>.

195

### 196 **3 Characteristics of the field experiment**

#### 197 **3.1 MODIS Aerosol optical depth and Weather conditions**

198 Figures 2a and b visualizes the numerous fire hotspots and high aerosol optical depth  
199 on 17 March 2018 registered by the MODIS satellite. Indeed, a large number of BB fire  
200 hotspots frequently occurred over Indochina during the springtime (Lin et al. 2009;  
201 2014) and EMeRGe-Asia campaign (supplementary Figure S1). On 17 March 2018 at  
202 06:00 UTC (14:00 LT; LT = UTC+8:00) the weather data indicated a series of high-  
203 pressure systems in northern China and a separate high-pressure system over Korea  
204 (Fig. 2c). At 1000 hPa, a strong northerly continental outflow was identified over  
205 southern Japan, the ECS, and Taiwan (Fig. 2d). On 19 March 2018, a new frontal  
206 system was located from Korea to the Guangdong province in SC (Fig. 2e). On the  
207 same day at 06:00 UTC, a discontinued flow was identified at the frontal zone to the  
208 north of Taiwan in the ECS (Fig. 2f). In other words, Taiwan was located at the  
209 prefrontal and warm conveyor area due to the surrounding southerly flow on 19 March  
210 2018 at 06:00 UTC (Figs. 2e and 2f, respectively). The southerly wind was gradually  
211 replaced by the northeasterly after another frontal passage on 20 March 2018 at 00:00  
212 UTC (data not shown).

213 In the upper layer (700 hPa; Figs. 2g–2j), the flow pattern differed from that at the  
214 near-ground surface (1000 hPa; Figs. 2d and 2f). A southwesterly strong wind, coming  
215 from the east side of the Tibetan Plateau in SC, moving to the North Eats i.e. Korea, is  
216 converted to a polar front wave flow in northeastern China and Korea on 17 March  
217 2018 (Fig. 2g). This high-elevation northward strong wind belt distribution at 700 hPa



218 was associated with a corresponding lee-side trough at the east of the Tibetan Plateau,  
219 whereas a ridge was noted over the east coast of China on the same day (Fig. 2h).  
220 Consistent with the mechanism reported by Lin et al. (2009), once a significant lee-side  
221 trough formed, it provided favorable conditions for the upward motion over the lee-side  
222 of the Tibetan Plateau and brought BB emission to the free troposphere layer following  
223 the strong wind belt transport to the downwind area. After the weather system moved  
224 to the east, the north–south trough turned to SW–NE such that the strong wind belt was  
225 in an approximately SW–NE direction and located between 20 and 30 °N on 19 March  
226 2018 (Figs. 2i and 2j). In conclusion, the Indochina BB pollutants were driven by the  
227 strong wind belt from Indochina, northward to SC on 17 March 2018 and then eastward  
228 passing over Taiwan between 20 and 30 °N to the south of Japan on 19 March 2018.

### 229 **3.2 Characteristics of LRT BB to the ECS by WRF-Chem model**

230 Figure 3 shows latitude longitude plots of the simulated CO concentration  
231 differences with and without BB emission at an elevation of 1000 m (Fig. 3a), mainly  
232 in Indochina, SC, and the South China Sea on 17 March 2018. The ambient flow was  
233 easterly and then northward from the South China Sea to SC at 1000 m elevation  
234 between 00:00 and 12:00 UTC on 17 March 2018 (Fig. 3a-b). The BB plume  
235 accumulated and persisted for an extended period in the lower part of the boundary  
236 layer on 17 and 19 March 2018 (Figs. 3a-b, and 3e-f). In contrast, the high CO  
237 concentration followed the southwesterly or westerly strong wind belt (Figs. 3c-d, and  
238 3g-h) and its weather conditions (Fig. 2) at an elevation of 3000-m (700 hPa). Following  
239 the movement of the ridge and trough at the 700 hPa geopotential height (Fig. 2h and  
240 2j), the associated strong wind belt turned to move eastward in the SW–NE direction  
241 between 17 and 19 March 2018. The BB plume transport over Indochina was affected  
242 by a fast-moving strong flow at 700 hPa (Fig. 2g and 2i), shifting the plume toward  
243 Taiwan and the ECS, during 17–19 March 2018. The highest CO concentration



244 contributed by the BB plume was >150 ppb, originally sourced from Indochina, and it  
245 was mainly transported northward on 17 March 2018 (Figs. 3c-d) and then covered a  
246 large area in East Asia at a CO concentration of >100 ppb on 19 March 2018 (Figs. 3g-  
247 h). Figure 4 indicates simulation differences for the contribution of BB along an E–W  
248 cross-section at 30 °N at 16:00 UTC on 18 March 2018 (Fig. 4a) and 06:00 UTC on 19  
249 March 2018 (Fig. 4b). We noted that a strong wind at 2000 m elevation and a high CO  
250 concentration (>70 ppb) due to BB at the BPTL. Moreover, the CO concentration  
251 attributed to BB was low at the elevation of >4000 m on 19 March at 06:00 UTC (Fig.  
252 4b), showing that the BB pollutants mainly affect altitudes below 4000 m.

### 253 3.3 Aircraft measurements

254 Two HALO flights were scheduled to the ECS to measure the pollutants following the  
255 continental outflow; the flights departed on 17 (Fig. 5a) and 19 (Fig. 6a) March 2018  
256 and followed similar tracks. To indicate the measurement results along the flight path,  
257 the 1-min average data is shown in Figures 5b and 6b. On 17 March 2018, the flight  
258 departed from Tainan (Fig. 1b) at 01:09 UTC (09:09 LT) first southbound and then  
259 northward to the ECS (Fig. 5a). The elevation for sample collection was mainly <4000  
260 m, where the CO concentration was found to be <200 ppb in most cases on that day  
261 (Fig. 5b). At elevations between 2000 and 4000 m, the concentration of the major  
262 aerosol components (i.e., OA, BC,  $\text{SO}_4^{2-}$ ,  $\text{NO}_3^-$ , and  $\text{NH}_4^+$ ) was mostly <2  $\mu\text{g m}^{-3}$ ,  
263 except just above western Taiwan after 08:00 UTC (Figs. 5a–5d). The peak  
264 concentrations for OA, BC,  $\text{SO}_4^{2-}$ ,  $\text{NH}_4^+$ , and  $\text{NO}_3^-$  were 3.4, 1.2, 2.1, and 0.7  $\mu\text{g m}^{-3}$ ,  
265 respectively, at the altitude between 2000 and 4000 m.  $\text{SO}_4^{2-}$  demonstrated the highest  
266 concentration among the aerosol components, especially during 04:00–04:37 and  
267 05:48–06:15 UTC (peaking at 5.1  $\mu\text{g m}^{-3}$ ) when the flight was north of 30 °N and an  
268 elevation of <1000 m (Figs. 5a–5c). This result could be attributed to anthropogenic  
269 pollution from the continental outflow (Lin et al. 2012) or probably part from Japan



270 contributed to the high sulfate concentration in the boundary layer over the ECS. As for  
271 the trace gases such as ACE, ACN and O<sub>3</sub>, their concentrations between 2000 and 4000  
272 m were stable and ranged between 1-2 ppb, 0.1-0.3 ppb, and 60-70 ppb (Fig. 5b),  
273 respectively, implying minor influence over the ECS by the BB plume in this flight.  
274 Figure 5e illustrates the HYSPLIT (Stein et al., 2021) 96-h backward trajectories, which  
275 identified the air mass origin starting at 02:00 UTC, followed by 04:00, 06:00, and  
276 09:00 UTC. The continental outflow contributed to higher sulfate concentrations (3–5  
277  $\mu\text{g m}^{-3}$  at 33 °N) at 04:00 and 06:00 UTC (Figs. 5b, 5c, and 5e) at <1000 m along the  
278 flight path. In contrast, south of 25 °N and above Taiwan, the local pollution and  
279 continental outflow are dominating sources on 17 March 2018.

280 The HALO flight on 19 March 2018 departed at 00:19 UTC (08:19 LT). It was  
281 bound northward and sampled air at an altitude of <4000 m most of the time, as shown  
282 in Figures 6a and 6b. Figures 6c and 6d indicate the latitude-height variation of SO<sub>4</sub><sup>2-</sup>  
283 and OA mass concentrations along the flight path on 19 March 2018. As the flight left  
284 Taiwan, it maintained an elevation of 3000 m during 01:00–02:00 UTC (Fig. 6a, 121–  
285 126 °E) and then descended to <1000 m during 02:00–02:40 UTC (Fig. 6b). The OA  
286 mass concentration was higher at 3000 m than at the low altitude during 01:00–03:00  
287 UTC (Figs. 6b and 6d). In particular, CO, OA and BC exhibited a substantial peak  
288 concentration of 312 ppb, 6.4  $\mu\text{g m}^{-3}$  and 2.5  $\mu\text{g m}^{-3}$  at 01:54 and 02:51 UTC at 26 °N,  
289 125–126 °E, and an altitude of 2000–4000 m, where a BPTL was observed. The trace  
290 gases such as ACE, ACN, and even O<sub>3</sub> (Fig. 6b) have consistent peak times in the BPTL  
291 with concentrations of 3.0 ppb, 0.6 ppb, and 79 ppb, respectively. In this flight, SO<sub>4</sub><sup>2-</sup>  
292 had the second-highest concentration among the aerosol components (1–2.4  $\mu\text{g m}^{-3}$ ;  
293 Figs. 6b and 6c) upstream of Taiwan (25–27 °N) during 1:00–3:00 UTC.

294 In the northern part of the flight between 03:00 and 05:00 UTC at an elevation of  
295 >3000 m, the aerosol component concentrations were all at their lowest level (Figs. 6b–



296 6d). During 05:00–07:00 UTC, the HALO aircraft flew back southward to 25 °N, where  
297 high OA mass concentrations appeared again between 2000 and 4000 m (Figs. 6a, 6b,  
298 and 6d). Sulfate was the species with the highest concentration between 05:30 and  
299 06:30 UTC (Figs. 6b and 6c) when the flight's elevation was <1000 m in the lower  
300 boundary between 25 and 27 °N (upstream of Taiwan). The reason explaining this  
301 observation is that the transport of anthropogenic pollutants of continental origin takes  
302 place mainly in the boundary layer (Figs. 6b–6d). Other aerosol species, such as NO<sub>3</sub><sup>-</sup>  
303 and NH<sub>4</sub><sup>+</sup>, demonstrated low concentrations, except when the elevation was <1000 m,  
304 where they ranged up to 1 μg m<sup>-3</sup> (Fig. 6b).

305 The 96-h HYSPLIT backward trajectory starting from the flight locations at  
306 02:00–07:00 UTC (Fig. 6e) indicated that the air masses at elevations between 2000  
307 and 4000 m were potentially transported from Indochina. North of 30 °N and at altitudes  
308 of >3000 m at 04:00 UTC, the concentrations of air pollutants (including OA, SO<sub>4</sub><sup>2-</sup>,  
309 NO<sub>3</sub><sup>-</sup>, and NH<sub>4</sub><sup>+</sup>) were low (Figs. 6b and 6e) even though the air mass in the low  
310 boundary was sourced from SC and the Taiwan Strait. In general, the results are  
311 consistent with those of Lin et al. (2009, 2014), Carmical et al. (2003), and Tang et al.  
312 (2003): the BPTL was mainly located south of 30 °N. The fact that higher OA was  
313 observed rather in the higher altitudes than in the lower boundary also demonstrated  
314 the vertical distribution over the ECS.

315 Figure 7 displays the vertical distribution of the gases and major aerosol  
316 components found on the flights on 17 (blue) and 19 (green) March 2018 as well as the  
317 mean concentrations noted in the seven flights (on 17, 19, 22, 24, 26, and 30 March and  
318 4 April 2018; red) to the ECS during EMERGE-Asia. Figure 7 illustrates all profiles  
319 calculated as 1-min mean and every 500-m interval with one standard deviation ( $\pm\sigma$ ).  
320 The number of the data points is displayed on the right side of each figure. The mean  
321 CO concentration profile demonstrated a decreasing trend from 240 ppb near the



322 ground to 150 ppb at an altitude of 2500 m and 140–160 ppb at altitudes >6000 m (Fig.  
323 7a). The concentration for 17 March 2018 (flight F0317) was similar to the mean  
324 concentration profile, except for that at the <1500 m elevation in the lower boundary.  
325 However, a higher CO concentration (40–80 ppb) enhancement was noted on 19 March  
326 2018 (flight F0319) than the mean profile and flight F0317. The mean difference in CO  
327 concentration between flights F0319 and F0317 was as high as 80 ppb at an elevation  
328 of 3000–3500 m (Fig. 7a). Similarly, OA concentration was significantly higher in the  
329 BPTL vertical distribution in flight F0319 than in the mean profile and flight F0317  
330 (Fig. 7b). The mean OA concentration for the flight F0319 peaked at an elevation of  
331 2000–2500 m, increasing to  $2 \mu\text{g m}^{-3}$  more than in the mean profile and flight F0317.  
332 Other aerosol components such as  $\text{SO}_4^{2-}$ ,  $\text{NH}_4^+$ , and  $\text{NO}_3^-$  (Supplementary Fig. S2a-c)  
333 also had a similar vertical distribution trend, but the concentration differences were  
334 minor compared with OA concentrations. The magnitude of the maximum differences  
335 between the flights F0319 and F0317 in the BPTL was 1.3, 0.7, and  $0.4 \mu\text{g m}^{-3}$  for  
336  $\text{SO}_4^{2-}$ ,  $\text{NH}_4^+$ , and  $\text{NO}_3^-$ , respectively. The maximum difference concentration of BC can  
337 be as high as  $1.2 \mu\text{g m}^{-3}$  at 2000–2500 m between the flights F0319 and F0317 (Fig.7c).  
338 Regarding the variation in hydrocarbon species such as ACN (Fig. 7d) and ACE ( Fig.  
339 7e) in the BPTL, their maximum mean concentrations in the flight F0319 were higher  
340 than those in the profile of the flight F0317 by 0.18 and 0.9 ppb, respectively. In other  
341 words, flight F0319 had a more significant impact on the CO, OA, BC, and volatile  
342 organic compound (VOC) species such as ACN and ACE in the BPTL, which might  
343 account for the effect of BB emission transport from Indochina. The ozone  
344 concentration was lower in both flights F0317 and F0319 than in the mean profile at  
345 the elevations <2000 m (Fig. 7f). The ozone titration by  $\text{NO}_x$  in the low boundary might  
346 also play a role. However, it was approximately 5–7 ppb higher in the flight F0319 than  
347 in the flight F0317 between the elevations of 1500 and 3000 m. In their downwind area,



348 LRT of BB emissions might increase this concentration further at the BPTL (Tang et  
349 al., 2003; Lin et al., 2014) and also discussed in section 4. By contrast, the J value  
350  $[J(O_1D)]$  (Fig. 7g) was higher for flight F0317 than for F0319 in the elevation range 1000–  
351 3000 m, in line with high aerosol concentrations and associated cloud enhancement that  
352 typically lead to decreased photolysis frequencies [i.e.,  $J(O_1D)$ ] (Tang et al., 2003).  
353 Consistently, at altitudes >4000 m the presence of clouds below the aircraft led to greater J  
354 values. The concentrations of other species such as  $NO_y$  (Fig.7h) and HONO  
355 (Supplementary Fig. S2d) were also greater in flight F0317 than in flight F0319 by 0.4–  
356 1.2 ppb and 10–34 ppt, respectively, in the low boundary (<1500 m). At the BPTL, the  
357 concentration of  $NO_y$  (1–2 ppb) in the flight F0319 was higher than in the flight F0317,  
358 but the difference was less than 0.6 ppb. The results from the TRACE-P campaign,  
359 which examined the Asian outflow of  $NO_y$ , also demonstrated large increases in  $NO_y$   
360 concentrations (0.5–1 ppb) downwind from Asia. The  $NO_y$  consisted mainly of  $HNO_3$   
361 and peroxyacetyl nitrate (Miyazaki et al., 2003; Talbot et al., 2003).

362

## 363 **4 Simulation results and discussion**

### 364 **4.1 Model performance and BB transport identification**

365 Tables 1 and 2 and Fig. 8 plot the Pearson correlation coefficients between 5-min  
366 merged observations on board the HALO and the simulation for flights F0317 and  
367 F0319. Meteorological parameters such as potential temperature ( $\theta$ ), relative  
368 humidity (RH), and wind speed (WS) were all captured well by the model along the  
369 HALO flight path on the 2 days. The correlation coefficient (R) for meteorological  
370 parameters was high, ranging from 0.92 to 0.99 (Table 1). The strong correlation  
371 indicates the high representativeness of the reanalysis of meteorological data used in  
372 the simulation. Among the trace species and aerosol components, toluene (TOL),  $NO_x$ ,  
373 ketones (KET), BC, OA, HONO,  $SO_2$ , and HCHO demonstrated an R of >0.5 (good



374 correlation) and CO and O<sub>3</sub> showed an R of nearly 0.5 (Table 1). The simulation  
375 performance was investigated in the BL (<1000 m; Fig. 8), at 2000–4000 m altitude  
376 (Table 2 and Fig. 8) and for the whole period of both flights (Table 1 and Fig. 8; blue  
377 dot). Even in the BPTL, the simulated meteorological parameters presented a good  
378 correlation (R > 0.93), followed by KET, OA, BC and CO (R > 0.6) as well as O<sub>3</sub> and  
379 NO<sub>y</sub> (R > 0.5) (Table 2). In other words, at the BPTL, the R for the simulation  
380 significantly increased for OA, BC, CO, and KET (Tables 1 and 2 and Fig. 8), which  
381 are indicators for BB being a source of pollution in the model. In contrast, SO<sub>4</sub><sup>2-</sup>, NO<sub>3</sub><sup>-</sup>,  
382 NH<sub>4</sub><sup>+</sup>, SO<sub>2</sub>, NO<sub>2</sub>, and HCHO had better correlation in the lower part of the boundary  
383 layer, at altitudes <1000 m (see Fig. 8) than in the BPTL. We explain this by the  
384 transport of anthropogenic pollutants in the continental outflow in the lower part of the  
385 boundary layer in ECS.

386 The modeling results tended to overestimate the concentration of the species, with  
387 examples being CO (59 ppb), OA (0.5 μg m<sup>-3</sup>), BC (0.3 μg m<sup>-3</sup>) and O<sub>3</sub> (12.1 ppb;  
388 Table 2) in the BPTL. Because high concentrations of CO, BC and OA in BPTL are  
389 accurate indicators of BB in the model, the BB emission from the source of FINN data  
390 are probably also overestimated (Lin et al., 2014). Except for OA and BC, the  
391 correlations for other aerosol components such as NH<sub>4</sub><sup>+</sup>, NO<sub>3</sub><sup>-</sup>, and SO<sub>4</sub><sup>2-</sup> were poor  
392 (0.23, 0.13, and -0.14, respectively). The poor correlation for SO<sub>4</sub><sup>2-</sup> may result from  
393 the large uncertainty in the emission of SO<sub>2</sub>.

394 Because the meteorological parameters were simulated well, the simulation  
395 discrepancies for chemical species are either caused by the emission estimation  
396 uncertainties or by inaccuracies in the simulation of chemical oxidation processes  
397 during LRT. Because CO, OA, and BC are accurate indicators of simulated BB  
398 transport from Indochina (Carmical et al., 2003), the airborne measurements on board  
399 the HALO are used as reference to evaluate the performance of the model for the flight



400 F0319 (Fig. 9). The 5-min merged simulation of CO concentration with (blue line) and  
401 without (green line) BB was compared to that measured on board the HALO (red line);  
402 the concentration was mostly in the range of 100–200 ppb, with its peak approaching  
403 300 ppb (at 01:50, 02:50, and 04:00 UTC) at the BPTL (Fig. 9a). In general, the  
404 simulation captured the CO variation along the flight path. However, it overestimated  
405 the observations by nearly 100 ppb for the simulation with BB at the BPTL during  
406 01:00–02:00, 03:40–04:20, 05:00–05:40, and 06:30–07:20 UTC (Fig. 9a). Notably, the  
407 simulation difference was minor when the flight was in the lower part of the boundary  
408 layer (02:30 and 06:00 UTC) i.e. < 1000m or at elevations of >4000 m (03:00–03:30  
409 and 04:20–05:00 UTC). The model underestimated CO concentration in the lower part  
410 of the boundary (<1000 m) (02:30 and 05:50–06:30 UTC) over the ECS. In conclusion,  
411 our model simulation overestimates BB emissions but underestimates continental CO  
412 emissions from China due to the underestimation of the emission inventory of the  
413 MICS-Asia III (Kong et al.,2020) was adopted in this study.

414 OA and BC are also important BB indicators and were reasonably captured by the  
415 model before 03:00 UTC when the flight was south of 28 °N at elevations of <4000 m  
416 (Fig. 9 b-c). The time series of simulated OA and BC has peak concentrations of nearly  
417 4–5.5  $\mu\text{g m}^{-3}$  and 2  $\mu\text{g m}^{-3}$ , respectively, during HALO shuttle flights passing through  
418 the BPTL (2000–4000 m) around 01:50 and 02:50 UTC. When BB emission was not  
419 included in the simulation, the concentration peaks were not observed (see Fig. 9b-c,  
420 green plot). Similar to the simulated CO results, the simulated OA and BC overestimate  
421 the amounts of these species to the north of 30 °N at 04:00 UTC (Fig. 6a and 9). The  
422 model after 07:30 UTC, which was related to local emission before HALO landed over  
423 western Taiwan on 19 March 2018. In general, our model simulation captured  
424 reasonably well OA and BC with an R of 0.55 and 0.68, respectively. A minor mean  
425 bias for OA (BC) is 0.4  $\mu\text{g m}^{-3}$  (0.2  $\mu\text{g m}^{-3}$ ) and the root mean square error (RMSE) of



426 OA (BC) is  $1.2 \mu\text{g m}^{-3}$  ( $0.4 \mu\text{g m}^{-3}$ ) (Table 1). The R for OA (BC) reached 0.69 (0.71),  
427 with an RMSE of  $1.0 \mu\text{g m}^{-3}$  ( $0.5 \mu\text{g m}^{-3}$ ) when we calculated the BB transport layer  
428 only between 2000 and 4000 m (Table 2 and Fig. 8). In addition to OA and BC,  
429 simulated aerosol species such as  $\text{SO}_4^{2-}$ , and  $\text{NH}_4^+$  were overestimated, whereas  $\text{NO}_3^-$   
430 was underestimated although their concentrations were low (Table 2). Because the  
431 BPTL was mainly between altitudes of 2000 and 4000 m, the subsequent discussion  
432 focuses on the influence of the BPTL from Indochina on the downstream areas,  
433 particularly the ECS and Taiwan.

#### 434 **4.2 Effects of LRT BB plume from Indochina on East Asia**

435 To investigate the regional impacts of BB plume transport from Indochina, we  
436 compared the simulation with and without BB emission for the events on 17 and 19  
437 March 2018. The analysis of the calculations focused on the impact over SC, Taiwan  
438 and ECS. These three selected regions are SCA (in South China), TWA (covered the  
439 whole Taiwan), and ECSA (in the ECS) as shown in Figure 1a. After being emitted the  
440 BB pollutants from Indochina were then transported northward to China and  
441 subsequently northeastward. The exact flow pattern depended on the weather  
442 conditions and flow types (ridge or trough) at 700 hPa (3000 m) between 17 and 19  
443 March 2018 (see Fig. 2). Consequently, we investigated the hourly variation in the area  
444 mean concentrations or mixing ratios of air pollutant trace constituents to assess the  
445 importance of BB emissions from Indochina on the selected downstream region e.g. the  
446 ECSA (Fig. 10), SCA, TWA and ECSA (Table 3). The contribution of CO (or others  
447 species) due to BB was estimated by detrainning the difference between simulations with  
448 and without the BB emission. These differences are then expressed as a fraction in  
449 percentage shown in Figure 10 (blue line). The mean concentration of CO (red line)  
450 over the ECSA (Fig. 10a) was at its lowest (115 ppb) on 17 March 2018; it gradually  
451 increased to a peak concentration of 280 ppb on 18 March 2018 and then remained



452 stable at 260 ppb on 19 March 2018. The contribution of CO from BB (blue line) ranged  
453 from 19 % (<22 ppb) on 17 March 2018 to a peak of 42 % (~113 ppb) on 18 March  
454 2018 and then gradually declined to 26 % on 19 March 2018 (Fig. 10a). As for OA  
455 (BC), the lowest percent contribution by BB was 14-16% (<5%) between 16 and 17  
456 March 2018 while the highest could be more than 30% (60%) during 18 and 19 March  
457 2018 (Fig. 10b and c). The variation trend of PM<sub>2.5</sub> its lowest percent contribution by  
458 BB was 21 % (0.42  $\mu\text{g m}^{-3}$ ) on 17 March 2018 (Fig. 10d), increasing to 40 % (5.6  $\mu\text{g}$   
459  $\text{m}^{-3}$ ) on 18 March 2018 because the BB plume spread by the strong wind to the ECSA.

460 The variation of O<sub>3</sub> (Fig. 10e) depends on transport and photochemistry, which  
461 involves the precursors NO<sub>x</sub> and VOC and the photolysis frequency of NO<sub>2</sub>, J(NO<sub>2</sub>).  
462 For the elevations between 2000–4000 m, O<sub>3</sub> changes are similar to those of CO, NO<sub>x</sub>  
463 and KET, which were mainly contributed by the LRT BB plume and related to the  
464 ozone precursor after 18 March 2018. The lowest and highest O<sub>3</sub> concentrations on 17  
465 and 18 March 2018 were 56 and 75 ppb, respectively, of which we estimate that 5.6  
466 ppb (10 %) and 34 ppb (45 %) were BB's contributions, respectively. Although the  
467 mean NO<sub>x</sub> concentration was relatively small (0.06–0.18 ppb), the BB contributed 35–  
468 70 % (0.02–0.13 ppb) during 17–19 March 2018 (Supplementary Fig. S3a). The KET  
469 concentration was in the range 0.4 to 2.7 ppb, with BB contributing nearly 20–26 %  
470 (0.08–0.7 ppb) during 17–19 March 2018 (Supplementary Fig. S3b).

471 The area-mean OH contributed by BB increased from its lowest level (<30 %) on  
472 17 March 2018 to its highest (nearly 70 %) on 19 March 2018 (Fig. 10f). HO<sub>2</sub> was also  
473 observed to increase trend from 10 % to 40 % during daytime over the period 17–19  
474 March 2018 (Supplementary Fig. S3c). The amounts of the oxidizing agent, OH, and  
475 the free radical HO<sub>2</sub> depend on the amounts of trace gases, which produce and remove  
476 these radicals, (eg. NO<sub>x</sub>, water vapor, ozone, hydrocarbons, etc.) and the relevant  
477 photolysis frequencies J(O<sub>3</sub>→O1D), J(NO<sub>2</sub>) etc.. Thus trace constituents from BB were



478 expected to increase OH and HO<sub>2</sub>. However, BB's contribution to photolysis  
479 frequencies  $J(\text{O}_3 \rightarrow \text{O}^1\text{D})$  (Fig. 10g),  $J(\text{NO}_2)$  (Supplementary Fig. S3d) etc. decreased  
480 as the mean BB aerosol concentration increased over the ECS during 17–19 March  
481 2018. This is because photolysis calculation results used simulated aerosol and cloud  
482 formation, which increased over the ECSA (Fig. 12).

483 The NO<sub>y</sub>, mean concentration ranged from 1.0 to 4.5 ppb, of which BB's  
484 contribution was from 55 to 82 % (Supplementary Fig. S3e). Such a high contribution  
485 from BB also demonstrated the effects of long-distance transport. Figure 10h indicates  
486 an increasing trend of HCHO concentration from 17 to 19 March 2018. HCHO  
487 formation and destruction depend on the rate of reaction of OH with HCHO precursors  
488 and the rate of reaction of HCHO with OH and the photolysis frequency of HCHO. As  
489 a result, HCHO production varied with OH concentration. The lowest and highest  
490 concentrations of HCHO were on 17 and 19 March 2018, respectively. In summary,  
491 the consistent variations in BB contributions to CO, PM<sub>2.5</sub>, VOC, OH, NO<sub>x</sub>, NO<sub>y</sub>, and  
492 O<sub>3</sub> peaked on 18 or 19 March 2018, whereas  $J(\text{O}^1\text{D})$  decreased between 17 and 19  
493 March 2018.

494 Figure 11 displays the fraction in % that the long-range transported BB emission  
495 contributes to the amounts of NO<sub>x</sub>, NO<sub>y</sub>, PM<sub>2.5</sub>, OA, BC, OH, O<sub>3</sub>, CO, KET, HO<sub>2</sub>,  
496 HCHO and  $J(\text{O}^1\text{D})$ , over the ECSA on 17 and 19 March 2018. Except for NO<sub>y</sub>, BB  
497 contribution was generally <11 % at elevations of <1000 m over the ECSA. The scatter  
498 distribution of the simulation results indicates that the effect of BB emission at  
499 elevations of <1000 m (Fig. 11a) was significantly lower than that between the  
500 elevations of 2000 and 4000 m (Fig. 11b). For NO<sub>y</sub>, NO<sub>x</sub>, PM<sub>2.5</sub>, BC, OH, O<sub>3</sub>, and CO,  
501 the BB contribution was >30 % at the elevation of 2000–4000 m over the ECSA (Fig.  
502 11b). Table 3 further summarizes the effect of BB emission on the downwind areas  
503 (SCA, TWA, and the ECSA) at the <1000 m and 2000–4000 m elevations. The



504 contribution of BB to  $\text{NO}_y$ ,  $\text{NO}_x$ ,  $\text{PM}_{2.5}$ , BC, OH,  $\text{O}_3$  and CO was at least 30–80 % at  
505 the elevation of 2000–4000 m over the regions SCA, TWA and ECSA. In the lower  
506 boundary layer (i.e. <1000 m), the BB contribution for most species at the remote  
507 downstream areas was <20 %, except for TWA. Because of the high mountains (Lin et  
508 al. 2021) present in TWA, the BB plume passing over Taiwan was potentially  
509 transported downward through mountain–valley circulation to the lower boundary layer  
510 (Ooi et al., 2021). The influence of BB over TWA was the highest among these three  
511 downstream regions (see Table 3) as its location was directly on the transport pathway  
512 for the BB plume on the major event day (flight F0319).

513 Figure 12 displays the simulated cloud water difference with and without BB  
514 emission over different regions on 17 and 19 March 2018. BB aerosols are a potential  
515 source of cloud nuclei. The simulations show the impact of BB on cloud water  
516 enhancement (Fig. 12). Cloud water enhancement over SCA was associated with  
517 aerosol enhancement from the BB in the altitude range 1000–4000 m: the peak being  
518 2–2.5  $\text{mg kg}^{-1}$  at 2000 m on these 2 days (Fig. 12). The abundance of BB emissions  
519 transported from Indochina to SCA (Fig. 3) is expected to contribute to the high cloud  
520 water formation over SCA. Furthermore, the southerly flow (Fig. 3) that transports  
521 warm and moist air mass from the South China Sea may have favored cloud formation  
522 in flights F0317 and F0319. High cloud water related to BB can be seen in the  
523 simulations of these two days. In the remote ECSA regions, the cloud water  
524 substantially increased on 19 March 2018 (Fig. 12) compared to 17 March 2018  
525 because of a significant difference in BB emissions transported to the ECSA between  
526 17 and 19 March 2018 (Fig. 3). Similarly, the cloud water enhancement over Taiwan  
527 also only appeared on 19 March 2018 (Fig. 12). Furthermore, nearly no difference in  
528 the cloud water vertical distribution over the region IDCA (Fig. 1a) in Indochina was  
529 noted because in the Indochina region, spring is the dry season (Lin et al., 2009) and



530 thus unfavorable for cloud water formation. The simulated downward short wave flux  
531 at ground surface was 1-3% reduction over the regions ECSA and SCA (supplementary  
532 Fig. S4) during 18-19 March 2018. The combination of BB aerosols enhancement and  
533 increased cloud water results in shortwave radiation reduction, implying the possibility  
534 of regional climate change in East Asia driven by BB aerosols.

535

## 536 **5. Summary**

537 The BB during spring in Indochina has a significant impact on the chemistry and  
538 composition of the troposphere in the surrounding regions of East Asia. During the  
539 EMERGe campaign in Asia, atmospheric pollutants were measured on board the HALO  
540 aircraft. In this study, a minor long-range BB transport event was observed from  
541 Indochina on 17 March 2018 (flight F0317), followed by a major long-range BB  
542 transport event on 19 March 2018 (flight F0319). The impact on tropospheric trace  
543 constituent composition and the environment has been investigated.

544 During the major BB transport event F0319, the 1-min mean of the peak  
545 concentrations of the trace constituents CO, O<sub>3</sub>, ACE, ACN, OA and BC between the  
546 altitudes of 2000 and 4000 m over the ECS were 312.0 ppb, 79.0 ppb, 3.0 ppb, 0.6 ppb,  
547 6.4  $\mu\text{g m}^{-3}$ , 2.5  $\mu\text{g m}^{-3}$  respectively. In comparison during the F0317 event CO, O<sub>3</sub>,  
548 ACE, ACN, OA and BC were 203.0 ppb, 71.0 ppb, 2.0 ppb, 0.3 ppb, 3.4  $\mu\text{g m}^{-3}$ , 1.2  
549  $\mu\text{g m}^{-3}$  respectively.

550 When the elevation was <1000 m for both the F0317 and F0319 events, the sulfates,  
551 rather than OA, had the highest concentrations. The peak concentration could be as high  
552 as 5.1  $\mu\text{g m}^{-3}$  in the low boundary for the event F0317 in the ECS. This observation is  
553 most likely explained by a continental outflow from regions having fossil fuel  
554 combustion in the lower boundary layer over the ECS.

555 In this study, the WRF-Chem model was employed to evaluate the BB plume



556 transported from Indochina and its influence on the downstream areas including South  
557 China, Taiwan, and the ECS. The contribution of the BB plume for most species in the  
558 remote downstream areas was <20 % in the lower boundary layer (altitude <1000 m).  
559 In comparison, the contribution of long-range transported BB plume was 30–80 %, or  
560 even higher, for many of the trace constituents ( $\text{NO}_y$ ,  $\text{NO}_x$ , CO, OH,  $\text{O}_3$ , BC and  $\text{PM}_{2.5}$ )  
561 in the altitude range between 2000 and 4000 m for SC, Taiwan, and the ECS. The large  
562 influence of BB over Taiwan is most probably because the BB transport passes directly  
563 over Taiwan.

564 BB aerosols are potential sources of cloud nuclei. The WRF simulations estimate  
565 the effect of the BB plume on cloud water formation over SC and the ECS. We observe  
566 in the simulations cloud water enhancement over SC at elevations of 1000–4000 m.  
567 This increase of cloud water is consistent with an increase in aerosol, caused by BB  
568 emissions, transported from Indochina to SC. In remote regions of the ECS, the  
569 simulated cloud water was significantly larger during the major BB event on 19 March  
570 2018 than the minor BB event on 17 March 2018. The simulated decrease of the  
571 photolysis frequency ( $J(\text{O}^1\text{D})$  and  $J(\text{NO}_2)$ ) is attributed to the difference in aerosol  
572 concentrations and associated cloud enhancement between the two events over the ECS.  
573 This we explain by the significant differences in BB emissions transported to the ECS  
574 between the two events.

575 Interestingly, we found the combination of increased BB aerosol concentration  
576 and increased amounts of cloud water led to reductions in the amount of incoming  
577 shortwave radiation at the surface over the ECS and SC. This influences tropospheric  
578 chemistry and composition, regional climate, precipitation, ocean biogeochemistry,  
579 agriculture and human health.

580

581 ***Data availability***



582 The EMERGe data are available at the HALO database  
583 (<https://doi.org/10.17616/R39Q0T>, DLR, 2022) and can be accessed upon registration.  
584 Modeling data can be made available upon request to the corresponding author.

585 ***Author contribution***

586 CYL conceived the idea, analyzed the data, writing and editing of the manuscript. WNC  
587 and YYC run the model and analyzed the data. CKC joined the manuscript  
588 discussion. CYLiu provided the MODIS data. HZ and HS provided trace gases data. EF  
589 provided acetonitrile data. FO performed the ozone measurement. OOK, BAH and  
590 MLP were responsible for the BC measurement. KK and JS were responsible for C-  
591 ToF-MS measurements. JPB and MDAH led the EMERGe-Asia experiment. All  
592 authors have read and agree to the published version of the manuscript.

593 ***Competing interests***

594 The authors declare that they have no conflict of interest.

595 ***Acknowledgments:***

596 The accomplishment of this work has financial support from the Ministry of Science  
597 and Technology, Taiwan, under grants MOST 108-2111-M-001-002, 109-2111-M-001-  
598 004 and 110-2111-M-001-013. We thank to National Center for High-performance  
599 Computing (NCHC) for providing computational and storage resources.

600 The HALO deployment during EMERGe was funded by a consortium comprising the  
601 German Research Foundation (DFG) Priority Program HALO-SPP 1294, the Institute  
602 of Atmospheric Physics of DLR, the Max Planck Society (MPG), and the Helmholtz  
603 Association. Johannes Schneider and Katharina Kaiser acknowledge funding through  
604 the DFG (project no. 316589531).

605

606

607

608 **References:**

609 Ackermann, I. J., Hass, H., Memmsheimer, M., Ebel, A., Binkowski, F. S., and Shankar,  
610 U.: Modal aerosol dynamics model for Europe: development and first applications,  
611 Atmos. Environ., 32, 2981–2999, [https://doi.org/10.1016/S1352-2310\(98\)00006-5](https://doi.org/10.1016/S1352-2310(98)00006-5),  
612 1998.

613 Ahmadov, R., McKeen, S. A., Robinson, A. L., Bahreini, R., Middlebrook, A. M., de  
614 Gouw, J. A., Meagher, J., Hsie, E.-Y., Edgerton, E., Shaw, S., and Trainer, M.: A  
615 volatility basis set model for summertime secondary organic aerosols over the



- 616 eastern United States in 2006, *J. Geophys. Res.*, 117,  
617 <https://doi.org/10.1029/2011JD016831>, 2012.
- 618 Andrés Hernández, M. D., Hilboll, A., Ziereis, H., Förster, E., Krüger, O. O., Kaiser,  
619 K., Schneider, J., Barnaba, F., Vrekoussis, M., Schmidt, J., Huntrieser, H.,  
620 Blechschmidt, A.-M., George, M., Nenakhov, V., Harlass, T., Holanda, B. A., Wolf,  
621 J., Eirenschmalz, L., Krebsbach, M., Pöhlker, M. L., Kalisz Hedegaard, A. B., Mei,  
622 L., Pfeilsticker, K., Liu, Y., Koppmann, R., Schlager, H., Bohn, B., Schumann, U.,  
623 Richter, A., Schreiner, B., Sauer, D., Baumann, R., Mertens, M., Jöckel, P., Kilian,  
624 M., Stratmann, G., Pöhlker, C., Campanelli, M., Pandolfi, M., Sicard, M., Gómez-  
625 Amo, J. L., Pujadas, M., Bigge, K., Kluge, F., 770 Schwarz, A., Daskalakis, N.,  
626 Walter, D., Zahn, A., Pöschl, U., Bönisch, H., Borrmann, S., Platt, U. and Burrows,  
627 J. P.: Overview: On the transport and transformation of pollutants in the outflow of  
628 major population centres –observational data from the EMeRGe European intensive  
629 operational period in summer 2017. *Atmos. Chem. Phys.*, 22, 5877–5924,  
630 <https://doi.org/10.5194/acp-22-5877-2022>, 2022.
- 631 Carmichael, G. R., Tang, Y., Kurata, G., Uno, I., Streets, D., Woo, J.-H., Huang, H.,  
632 Yienger, J., Lefer, B., Shetter R. et al.: Regional-scale chemical transport modeling  
633 in support of the analysis of observations obtained during the TRACE-P experiment,  
634 *J. Geophys. Res.*, 108(D21), 8823, doi:10.1029/2002JD003117, 2003.
- 635 Chuang, M.T., Fu, J.S., Lee, C.T., Lin, N.H., Gao, Y., Wang, S.H., Sheu, G.R., Hsiao,  
636 T.C., Wang, J.L., Yen, M.C., Lin, T.H. and Thongboonchoo, N.: The simulation of  
637 long-range transport of biomass burning plume and short-range transport of  
638 anthropogenic pollutants to a mountain observatory in East Asia during the 7-  
639 SEAS/2010 Dongsha Experiment. *Aerosol Air Qual. Res.* 16: 2933–2949, 2016.
- 640 Chi K H., C. Y. Lin, C.F.Ouyang, J.Lin Lin, N.H. Lin, G.R. Sheu, C. T. Lee: PCDD/F  
641 Measurement at a High-altitude Station in Central Taiwan: Evaluation of Long-range  
642 Transport of PCDD/Fs during the Southeast Asia Biomass Burning Event,  
643 *Environmental Science & Technology*, 44, 2954-2960, DOI: 10.1021/es1000984  
644 <https://doi.org/10.1021/es1000984>, 2010.
- 645 Ding K., Huang X., Ding A., Wang M., Su H., et al.: Aerosol-boundary-layer-monsoon  
646 interactions amplify semi-direct effect of biomass smoke on low cloud formation in  
647 Southeast Asia., *Nature Communications*, 12:6416, 2021.
- 648 Fu, J. S., Hsu, N. C., Gao, Y., Huang, K., Li, C., Lin, N.-H., and Tsay, S.-C.: Evaluating  
649 the influences of biomass burning during 2006 BASE-ASIA: a regional chemical  
650 transport modeling, *Atmos. Chem. Phys.*, 12, 3837–3855,  
651 <https://doi.org/10.5194/acp-12-3837-2012>, 2012.
- 652 Galanter, M., Levy, H., Carmichael, G. R.: Impacts of biomass burning on tropospheric  
653 CO, NO<sub>x</sub>, and O<sub>3</sub>, *J. Geophys. Res. Atmos.*, 105, 6633-6653, 2000.



- 654 Giglio, L., Randerson, J.T., Werf, G.R.V.D.: Analysis of daily, monthly, and annual  
655 burned area using the fourth-generation global fire emissions database (GFED4). *J.*  
656 *Geophys. Res. Biogeosci.* 118 (1), 317–328., 2013.
- 657 Grell, G. A., Peckham, S. E., Schmitz, R., McKeen, S. A., Frost, G., Skamarock, W. C.,  
658 and Eder, B.: Fully coupled “online” chemistry within the WRF model, *Atmos.*  
659 *Environ.*, 39, 6957–6975, <https://doi.org/10.1016/j.atmosenv.2005.04.027>, 2005.
- 660 Heald, C. L., Jacob D.J., Fiore, A.M., Emmons, L. K., et al.: Asian outflow and trans-  
661 Pacific transport of carbon monoxide and ozone pollution: An integrated satellite,  
662 aircraft, and model perspective, *J. Geophys. Res.*, 108(D24), 4804,  
663 doi:10.1029/2003JD003507, 2003.
- 664 Hong, S., Lakshmi V., Small, E.E., Chen, F., Tewari, M., Manning, K.W.: Effects of  
665 vegetation and soil moisture on the simulated land surface processes from the  
666 coupled WRF/Noah model. *J Geophys Res* 114(D18), D18118, 2009.
- 667 Huang, K., Fu, J. S., Hsu, N.C., Gao, Y., Dong, X., Tsay, S. C., Lam, Y. F.: Impact  
668 assessment of biomass burning on air quality in Southeast and East Asia during  
669 BASE-ASIA, *Atmospheric Environment*, 78, 291e302, 2013.
- 670 Jacob, D.J., Crawford, J. H. Kleb, M. M., Connors, V. S, Bendura, R. J., Raper, J. L.,  
671 Sachse, G. W., Gille, J. C., Emmons, L., Heald, C. L.: The transport and chemical  
672 evolution over the pacific (trace-P) aircraft mission: design, execution, and first  
673 results. *J. Geophys. Res. Atmos.* 108 (D20), 2003.
- 674 Janjic, Z.I.: The step-mountain eta coordinate model: further developments of the  
675 convection, viscous layer, and turbulence closure schemes, *Mon. Wea. Rev.*, 122,  
676 927–945, 1994.
- 677 Kong L., Tang X., Zhu J., Wang Z., Fu J.S., Wang X., et al.: Evaluation and uncertainty  
678 investigation of the NO<sub>2</sub>, CO and NH<sub>3</sub> modeling over China under the framework  
679 of MICS-Asia III. *Atmos. Chem. Phys.*, 20, 181–202, 2020.  
680 <https://doi.org/10.5194/acp-20-181-2020>
- 681 Li, J., Nagashima, T., Kong, L., Ge, B., Yamaji, K., Fu, J. S., Wang X., Fan, Q., Itahashi,  
682 S., et al.: Model evaluation and inter-comparison of surface-level ozone and relevant  
683 species in East Asia in the context of MICS-ASIA phase III Part I: overview. *Atmos.*  
684 *Chem. Phys.*, 19, 12993–13015, <https://doi.org/10.5194/acp-19-12993-2019>, 2019.
- 685 Lin, C.Y., Hsu, H.M., Lee, Y.H., Kuo, C. H., Sheng, Y.F., Chu, D. A.: A new transport  
686 mechanism of biomass burning from Indochina as identified by modeling studies.,  
687 *Atmos. Chem. Phys.*, 9, 7901-7911. <https://doi.org/10.5194/acp-9-7901-2009>, 2009.
- 688 Lin, C. Y., Chou, C.C.K, Wang, Z., Lung, S.C., Lee, C. T., Yuan, C.S., Chen, W. N.,  
689 Chang, S. Y., Hsu, S. C., Chen, W. C., Liu, Shaw. C.: Impact of different transport  
690 mechanisms of Asian dust and anthropogenic pollutants to Taiwan. *Atmospheric*  
691 *Environment*, 60, 403-418, <http://dx.doi.org/10.1016/j.atmosenv.2012.06.049>, 2012.



- 692 Lin, C. Y., Zhao, Liu, C. X., Lin, N. H., Chen, W. N.: Modeling of long-range transport  
693 of Southeast Asia biomass burning pollutants to Taiwan and their radiative forcing  
694 over East Asia, *Tellus B*, 66, 1-17. 23733.  
695 <http://dx.doi.org/10.3402/tellusb.v66.23733>, 2014.
- 696 Lin, C.Y., Sheng, Y. F., Chen, W. C., Chou, C.C. K., Chien, Y. Y., Chen, W. M.: Air  
697 quality deterioration episode associated with typhoon over the complex topographic  
698 environment in central Taiwan. *Atmos. Chem. Phys.*, 21, 16839-16910.  
699 <https://doi.org/10.5194/acp-21-16893-2021>, 2021.
- 700 Lin, N.H., Tsay, S.C., Reid, J. S., Yen, M.C., Sheu, G. R., Wang, S.H., Chi, K.H., et al. :  
701 An overview of regional experiments on biomass burning aerosols and related  
702 pollutants in Southeast Asia: From BASE-ASIA and Dongsha Experiment to 7-  
703 SEAS. *Atmos. Environ.* 78: 1–19, 2012.
- 704 Marvin, M. R., Palmer P. I., Latter, B. G., Siddans, R., Kerridge, B.J., Latif, M. T., Khan,  
705 M. F.: Photochemical environment over Southeast Asia primed for hazardous ozone  
706 levels with influx of nitrogen oxides from seasonal biomass burning. *Atmos. Chem.*  
707 *Phys.*, 21, 1917–1935. <https://doi.org/10.5194/acp-21-1917-2021>, 2021.
- 708 Miyazaki Y., Kondo Y., Koike M., Fuelberg H. E., Kiley C. M., Kita K., Takegawa N.,  
709 Sachse G. W., Flocke F., Weinheimer A. J., Singh H. B., Eisele F. L., Zondlo M.,  
710 Talbot R. W., Sandholm S. T., Avery M. A., Blake D. R.: Synoptic-scale transport of  
711 reactive nitrogen over the western Pacific in spring, *J. Geophys. Res.*,  
712 108(D20),8788, doi:10.1029/2002JD003248., 2003.
- 713 Morrison H., Curry, J.A., Khvorostyanov, V.I.: A new double-moment microphysics  
714 parameterization for application in cloud and climate model. PartI: Description.  
715 *Journal of the Atmospheric Sciences.*, 62, 1665-1676, 2005.
- 716 Palmer, P. I., Jacob, D. J., Jones, D. B. A., Heald, C. L., Yantosca, R. M., Logan, J. A.,  
717 Sachse, G. W. and Streets, D. G.: Inverting for emissions of carbon monoxide from  
718 Asia using aircraft observations over the western Pacific, *J. Geophys. Res.*, 108(D21),  
719 8828, doi:10.1029/2003JD003397, 2003.
- 720 Pimonsree, S., Vongruang, P., Sumitsawan, S.: Modified biomass burning emission in  
721 modeling system with fire radiative power: Simulation of particulate matter in  
722 Mainland Southeast Asia during smog episode. *Atmospheric Pollution Research*, 9,  
723 133-145. <http://dx.doi.org/10.1016/j.apr.2017.08.002>, 2018.
- 724 Ramanathan, V., Ramana, M. V., Roberts, G., Kim, D., Corrigan, C., Chung, C., and  
725 Winker, D.: Warming trends in Asia amplified by brown cloud solar absorption.  
726 *Nature*, 448, 575-U575, 2007.
- 727 Reid, J. S., Hyer, E. J., Johnson, R. S., Holben, B. N., Yokelson, R. J., Zhang, J., et al. :  
728 Observing and understanding the Southeast Asian aerosol system by remote sensing:  
729 An initial review and analysis for the Seven Southeast Asian Studies (7SEAS)



730 program, Atmospheric Research, 122, 403-468, 2013.

731 Shi, Y., Yamaguchi, Y.: A high-resolution and multi-year emissions inventory for  
732 biomass burning in Southeast Asia during 2001-2010. Atmospheric Environment,  
733 98, 8-16, <http://dx.doi.org/10.1016/j.atmosenv.2014.08.050>, 2014.

734 Stein, A. F., R. R. Draxler, G. D. Rolph, B. J. B. Stunder, M. D. Cohen, and F.  
735 Ngan. : NOAA's HYSPLIT Atmospheric Transport and Dispersion Modeling  
736 System, Bulletin of the American Meteorological Society 96, 12 (2015): 2059-  
737 2077, <https://doi.org/10.1175/BAMS-D-14-00110.1>, 2021.

738 Stockwell, W. R., Middleton, P., Chang, J. S., and Tang, X.: The second generation  
739 regional acid deposition model chemical mechanism for regional air quality  
740 modeling, J. Geophys. Res., 95, 16343-16367, 1990.

741 Talbot, R., Dibb, J., Scheuer E., Seid G., Russo R., Sandholm S., Tan D., Singh H.,  
742 Blake D., Blake N., Atlas E., Sachse G., Jordan C., Avery M., 2003: Reactive  
743 nitrogen in Asian continental outflow over the western Pacific: Results from the  
744 NASA Transport and Chemical Evolution over the Pacific (TRACE-P) airborne  
745 mission. J. Geophys. Res., 108 (D20), doi:10.1029/2002JD003110, 2003.

746 Tang, Y., Carmichael, G. R., Woo, Jung-Hun, Thongboonchoo N., Kurata, G., Uno, I.,  
747 Streets D. G., et al.: Influences of biomass burning during the Transport and  
748 Chemical Evolution Over the Pacific (TRACE-P) experiment identified by the  
749 regional chemical transport model, J. Geophys. Res., 108(D21), 8824, 2003.

750 Wiedinmyer, C., Akagi, S. K., Yokelson, R. J., Emmons, L. K., Al-Saadi, J.A., Orlando,  
751 J. J., and Soja, A. J.: The Fire INventory from NCAR (FINN): a high resolution  
752 global model to estimate the emissions from open burning, *Geosci. Model Dev.*, **4**,  
753 625-641, doi:10.5194/gmd-4-625-2011, 2011.

754 Xu, R., Tie, X., Li, G., Zhao, S., Cao, J., Feng T., Long X., Effect of biomass burning  
755 on black carbon (BC) in South Asia and Tibetan Plateau: The analysis of WRF-Chem  
756 modeling. *Science of the Total Environment* , 645,901-912., 2018.

757 Yadav, I. C., Devi, N. L., Li, J., Syed, J. H., Zhang, G., Watanabe, H.: Biomass burning  
758 in Indo-China peninsula and its impacts on regional air quality and global climate  
759 change-a review. *Environmental Pollution*, 227, 414-427, 2017.

760 Zhao, C., Liu, X., Leung, L. R. and Hagos, S.: Radiative impact of mineral dust on  
761 monsoon precipitation variability over West Africa. *Atmos. Chem. Phys.*, **11**, 1879-  
762 1893, 2011.

763  
764  
765  
766  
767



768

769

770

771

772

773 Table 1 Observed and simulated mean values for bias (BIAS), root mean square error  
774 (RMSE), and correlation coefficients (R) for EMeRGe HALO flights on 17 and 19  
775 March 2018. KET\*: the observed Acetone is applied to compare with simulated ketones  
776 (KET).

	OBS_ave	SIM_ave	BIAS	RMSE	R
THETA(K)	304.8	304.2	-0.6	1.1	0.99
WS(m/s)	9.1	8.5	-0.6	2.0	0.94
RH(%)	63.6	63.0	-0.6	10.6	0.92
OA( $\mu\text{g}/\text{m}^3$ )	1.2	1.5	0.4	1.2	0.55
BC( $\mu\text{g}/\text{m}^3$ )	0.4	0.5	0.2	0.4	0.68
SO <sub>4</sub> <sup>2-</sup> ( $\mu\text{g}/\text{m}^3$ )	1.1	2.5	1.4	2.2	0.37
NO <sub>3</sub> ( $\mu\text{g}/\text{m}^3$ )	0.2	0.6	0.5	2.1	0.31
NH <sub>4</sub> <sup>+</sup> ( $\mu\text{g}/\text{m}^3$ )	0.4	0.7	0.3	1.1	0.49
CO(ppb)	170.8	188.9	18.1	69.6	0.46
SO <sub>2</sub> (ppb)	0.2	0.9	0.7	1.3	0.52
O <sub>3</sub> (ppb)	59.7	63.2	3.5	14.1	0.42
NO <sub>x</sub> (ppb)	0.2	0.2	0.0	0.2	0.74
NO <sub>2</sub> (ppb)	1.2	2.8	1.5	2.5	0.04
KET*(ppb)	1.4	1.5	0.1	0.9	0.59
TOL(ppb)	0.1	0.1	0.0	0.1	0.76
XYL(ppb)	0.1	0.0	0.0	0.1	0.38
HCHO(ppb)	0.1	0.7	0.6	0.7	0.50
HONO(ppt)	10.5	1.0	-9.4	15.4	0.55

777



778 Table 2 Observed and simulated mean values at an elevation between 2 km and 4 km  
779 for bias (BIAS), root mean square error (RMSE), and correlation coefficients (R) during  
780 EMERGe HALO flights on 17 and 19 March 2018. KET\*: the observed Acetone is  
781 applied to compare with simulated ketones (KET).

	OBS_ave	SIM_ave	BIAS	RMSE	R
THETA(K)	307.5	306.7	-0.8	0.9	0.98
WS(m/s)	8.2	7.9	-0.3	1.7	0.93
RH(%)	55.8	56.1	0.4	7.6	0.96
OA( $\mu\text{g}/\text{m}^3$ )	1.3	1.8	0.5	1.0	0.69
BC( $\mu\text{g}/\text{m}^3$ )	0.4	0.7	0.3	0.5	0.71
SO <sub>4</sub> <sup>2-</sup> ( $\mu\text{g}/\text{m}^3$ )	0.8	2.6	1.8	2.3	-0.14
NO <sub>3</sub> <sup>-</sup> ( $\mu\text{g}/\text{m}^3$ )	0.1	0.1	-0.1	0.4	0.13
NH <sub>4</sub> <sup>+</sup> ( $\mu\text{g}/\text{m}^3$ )	0.4	0.4	0.1	0.3	0.23
CO(ppb)	164.4	223.4	59.0	80.3	0.60
SO <sub>2</sub> (ppb)	0.0	1.0	1.0	1.2	-0.03
O <sub>3</sub> (ppb)	60.1	72.2	12.1	14.5	0.54
NO <sub>x</sub> (ppb)	0.1	0.2	0.0	0.1	0.54
NO <sub>y</sub> (ppb)	1.0	3.8	2.8	3.3	0.53
KET*(ppb)	1.5	1.9	0.4	0.9	0.71
TOL(ppb)	0.1	0.0	0.0	0.1	0.13
XYL(ppb)	0.0	0.0	0.0	0.0	-0.17
HCHO(ppb)	0.1	0.7	0.6	0.8	0.23
HONO(ppb)	6.0	0.6	-5.4	7.2	0.24

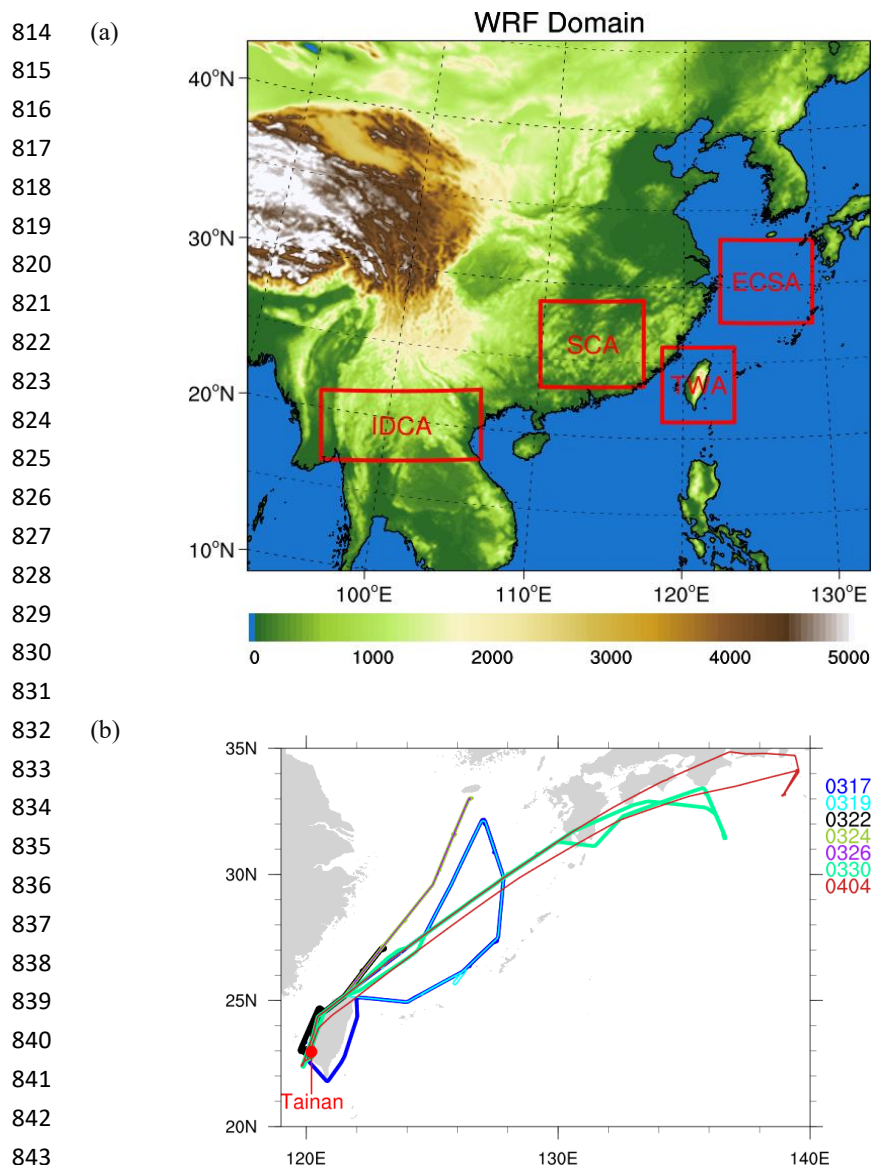
782  
783  
784  
785  
786  
787  
788  
789  
790  
791  
792  
793  
794  
795  
796  
797  
798  
799  
800  
801



802 Table 3: Simulated biomass burning contribution (with and without BB emission in  
803 Indochina) in percentage (%) on 17 and 19 March, 2018 for different regions: SCA,  
804 TWA, ECSA as shown in Figure 1a  
805

Average	SCA		TWA		ECSA	
	< 1KM	2-4KM	< 1KM	2-4KM	< 1KM	2-4KM
NO <sub>y</sub>	14.9	72.9	44.8	83.2	18.9	71.5
NO <sub>x</sub>	-1.4	58.1	3.7	70.8	2.1	51.2
PM <sub>2.5</sub>	5.8	44.6	14.7	56.4	7.2	31.9
OA	4.4	37.2	6.7	47.6	4.6	24.6
BC	6.9	74.4	14.0	81.0	6.1	42.4
OH	14.3	43.6	24.7	66.6	10.0	48.1
O <sub>3</sub>	18.8	33.7	23.5	38.5	9.4	31.0
CO	9.8	31.4	21.7	37.8	11.1	32.0
KET	6.0	17.0	9.0	26.8	7.0	24.5
HCHO	-3.5	10.2	-3.8	20.7	-4.0	10.3
HO <sub>2</sub>	9.0	4.5	15.4	35.5	6.4	24.9
J(O <sup>1</sup> D)	-3.0	-1.7	-1.1	0.4	-1.6	-1.1

806  
807  
808  
809  
810  
811  
812  
813

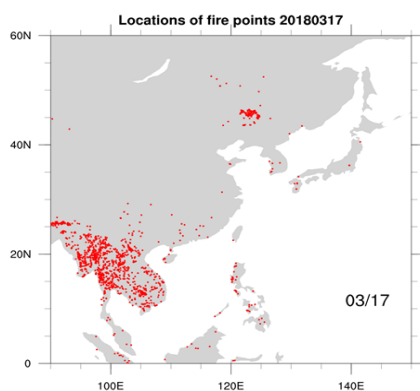


844 Figure 1 (a) Configuration of Weather Research and Forecasting model domain,  
845 topography, and location of proposed study areas in East Asia, namely IDCA (Indochina  
846 area), SCA (southern China area), TWA (Taiwan area) and ECSA (East China Sea area,  
847 respectively). (b) The HALO flights on 17, 19, 22, 24, 26, 30 March, and 04 April  
848 during EMeRGe Asia campaign. Different colors indicated different flights over East  
849 Asia. Maps and plots were produced using NCAR Command Language (NCL) version  
850 6.6.2.

851

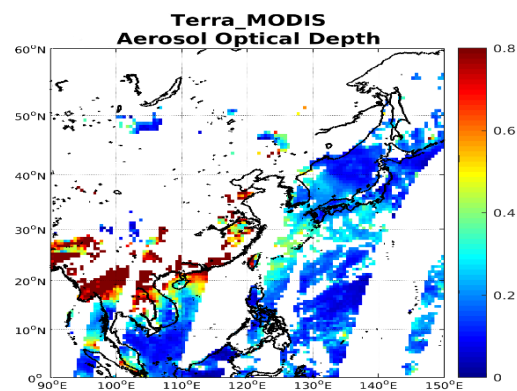


852 (a)



853

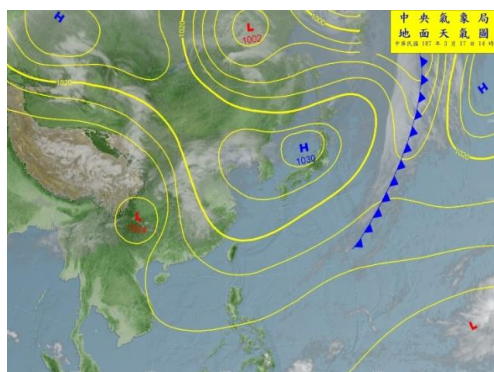
(b)



854

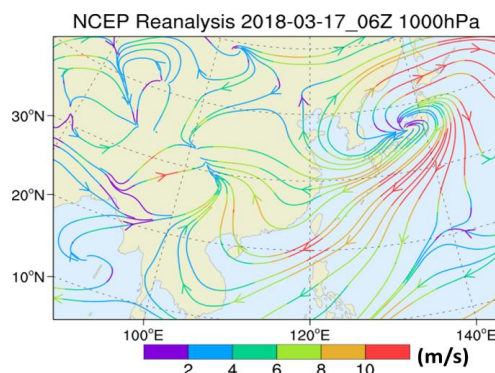
855 (c)

856



857

(d)



858 Fig.2 (a) MODIS fire hot spots on 17 March 2018 (source: [https://modis-](https://modis-fire.umd.edu/guides.html)  
859 [fire.umd.edu/guides.html](https://modis-fire.umd.edu/guides.html)) and (b) Composited Aerosol Optical Depth (AOD) from  
860 MODIS onboard NASA Terra satellite. The Collection 6.1 AOD is downloaded from  
861 NASA Earth Data website (<https://www.earthdata.nasa.gov/learn/find-data>), and  
862 composited for 0110, 0115, 0120, 0125, 0130, 0250, 0255, 0300, 0305, 0310, 0430,  
863 0435, 0440, 0445, 0610, 0615, 0620, 0745 and 0750UTC data granules on 17 March  
864 2018. (c) weather Chart at 06:00 UTC on 17 March 2018 (d) 1000 hPa streamlines at  
865 06:00 UTC, 17 March 2018 (e) and (f) same as (c) and (d) but on 19 March 2018 ;(g)  
866 700 hPa streamlines at 06:00 UTC, on 17 March 2018 (h) 700 hPa geopotential height  
867 at 06:00 UTC, on 17 March 2018; (i) and (j) same as (g) and (h) but on 19 March  
868 2018.

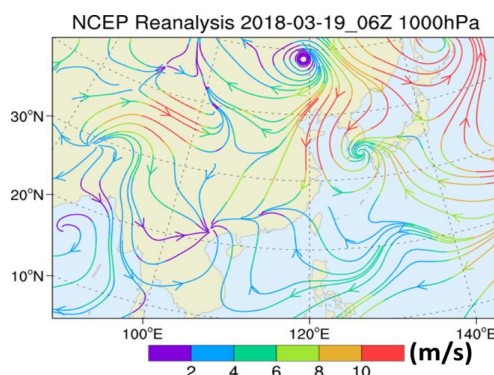
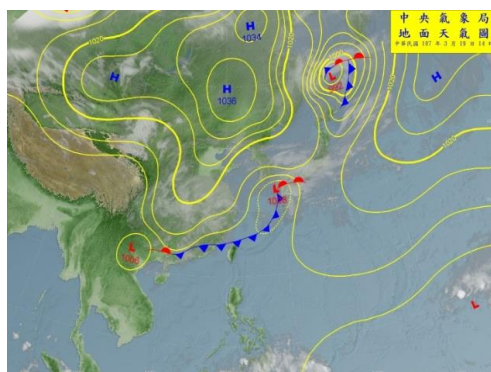
869 Near-surface weather charts and satellite images were provided by Central Weather  
870 Bureau (CWB) Taiwan. The near-surface and 700 hPa streamlines and geopotential



871 height were deduced from NCEP Reanalysis data. Maps and plots were produced using  
872 NCAR Command Language (NCL) version 6.6.2.

873

874 (e) (f)

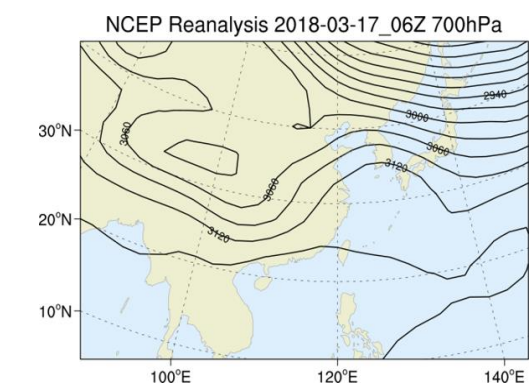
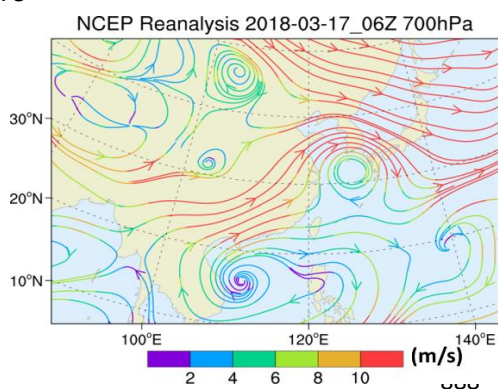


875

876

877 (g) (h)

878



889

890

891

892 Figure 2 e-h continued

893

894

895

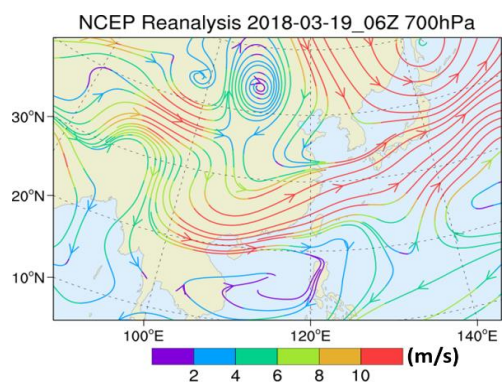
896

897

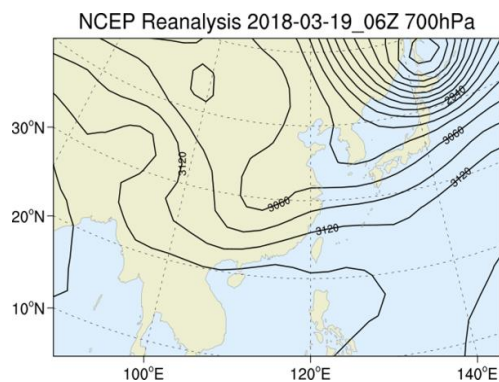
898 (i) (j)



899  
900

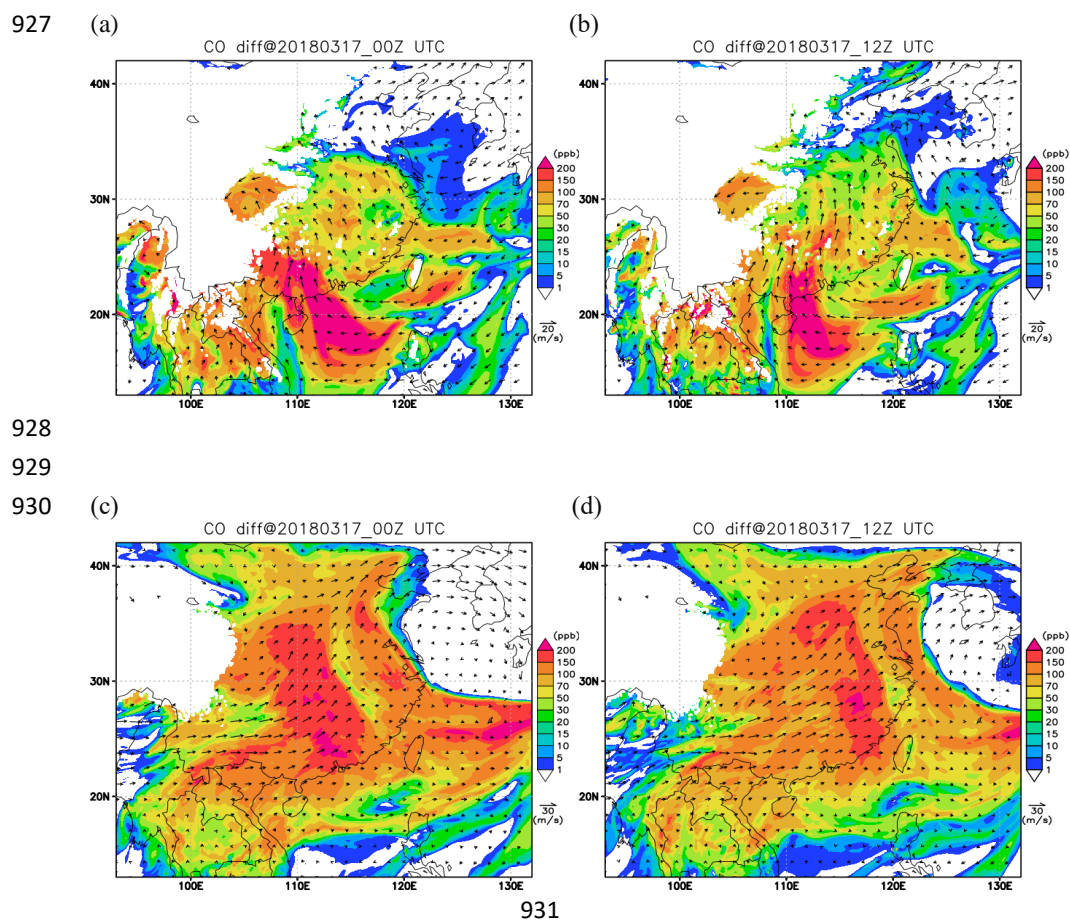


901



902  
903  
904  
905  
906  
907  
908  
909  
910  
911  
912  
913  
914  
915  
916  
917  
918  
919  
920  
921  
922  
923  
924  
925  
926

Fig. 2 i-j continued



932

933

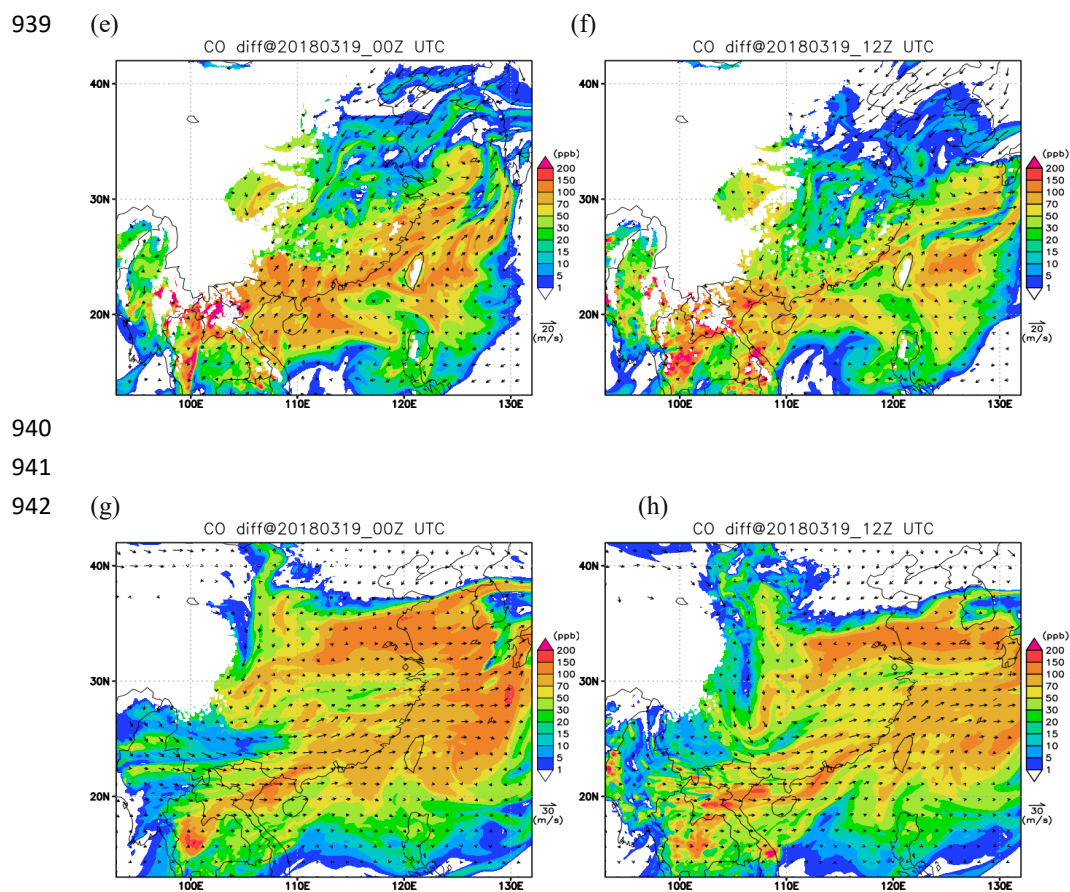
934 Fig 3 a-d : Simulated wind field ( $\text{m s}^{-1}$ ) distribution and concentration (unit: ppb)

935 difference with and without BB emission for CO on 17 March, 2018 at 00:00 UTC (a,

936 c) and 12:00 UTC (b, d) for 1km altitude (a, b) and 3km altitude (c, d). (unit:ppb)

937

938



943  
944 Fig 3 e-h: Simulated wind field ( $\text{m s}^{-1}$ ) and concentration (unit: ppb) difference with  
945 and without BB emission for CO on 19 March, 2018 at 00:00 UTC (e, g) and 12:00  
946 UTC (f, h) for 1km altitude (e, f) and 3km altitude (g, h).

947  
948  
949  
950  
951  
952  
953  
954  
955  
956  
957



958 (a)

959

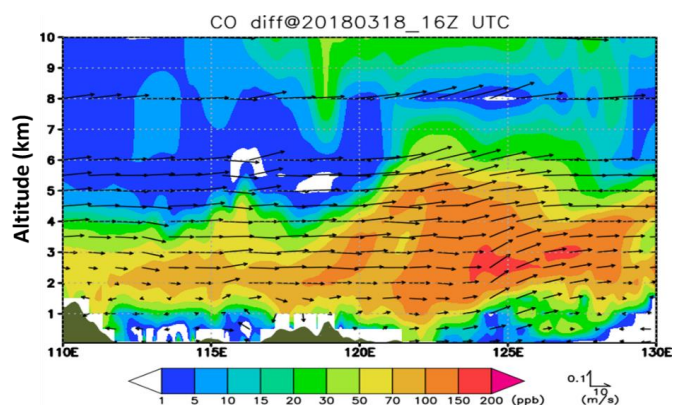
960

961

962

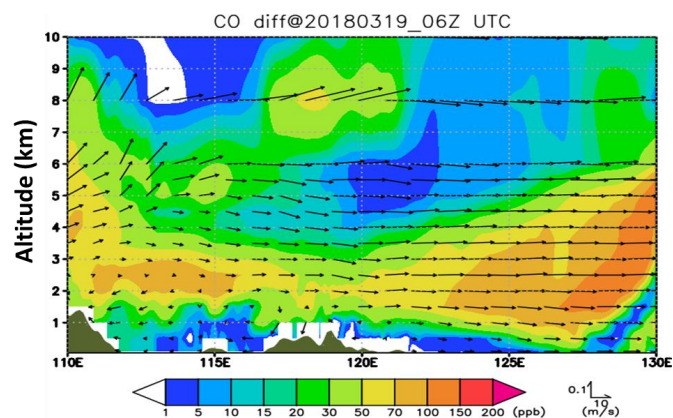
963

964



965

966 (b)



967

968

969

970

971 Fig. 4 Simulated wind field ( $\text{m s}^{-1}$ ) distribution and the concentration (ppb) difference

972 between with and without BB emission for CO at cross-section  $30^\circ\text{N}$  (a) 16:00 UTC

973 18 March 2018 (b) 06:00 UTC, 19 March 2018. Wind vectors represent along section

974 winds, with scales shown at the down-right corner of plot (unit:  $\text{m s}^{-1}$ )

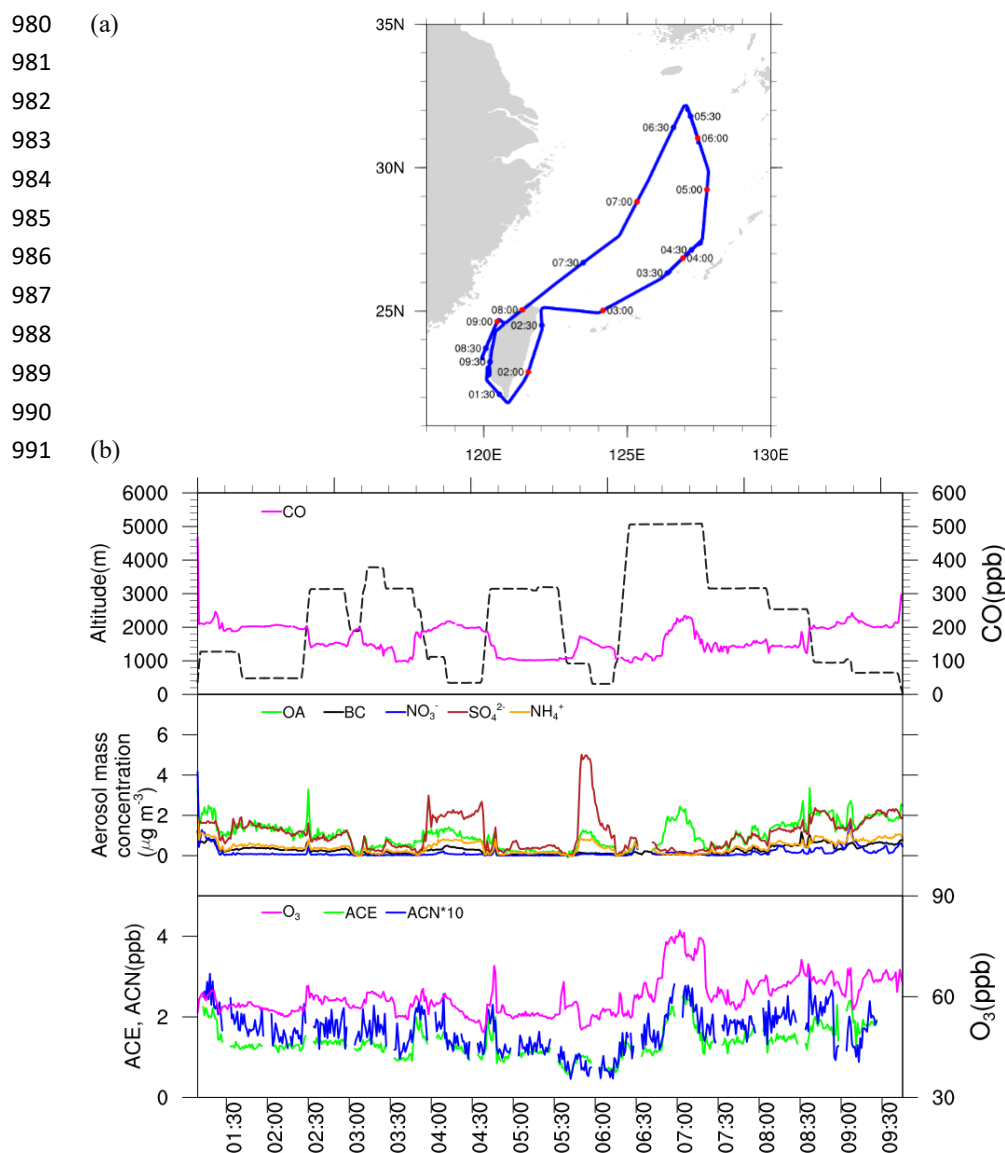
975

976

977

978

979



992

993 Fig. 5 (a) The HALO flight and detailed locations on 17 March 2018. (b) Flight altitude and 1-min mean of observed concentrations for CO (upper), Organic aerosol (OA), BC

994

995 aerosol (BC),  $\text{SO}_4^{2-}$ ,  $\text{NO}_3^-$ ,  $\text{NH}_4^+$  (middle),  $\text{O}_3$ , acetone (ACE) and acetonitrile (ACN)

996 (bottom) on 17 March. (c) The observed  $\text{SO}_4^{2-}$  mass concentration by HALO along with height-latitude variations on 17 March 2018 (d) The observed OA mass

997

998 concentration by HALO along with height-latitude variations on 17 March 2018 (e)

999 Result of the HYSPLIT model backward trajectory analysis started at the location of

1000 the HALO flight path at 02:00, 04:00, 06:00, 09:00 UTC on 17 March 2018.



1001 (c)

1002

1003

1004

1005

1006

1007

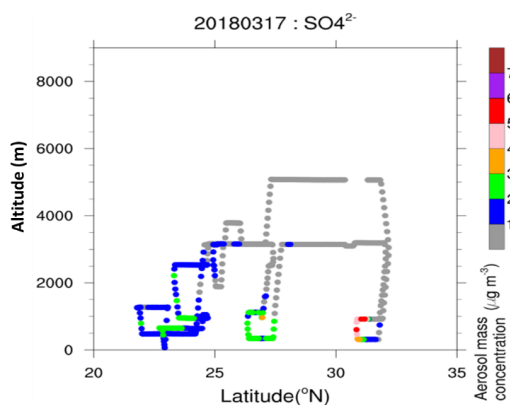
1008

1009

1010

1011

1012



1013 (d)

1014

1015

1016

1017

1018

1019

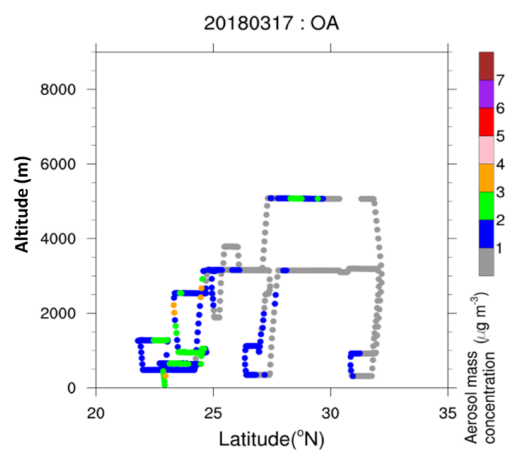
1020

1021

1022

1023

1024



1025 (e)

1026

1027

1028

1029

1030

1031

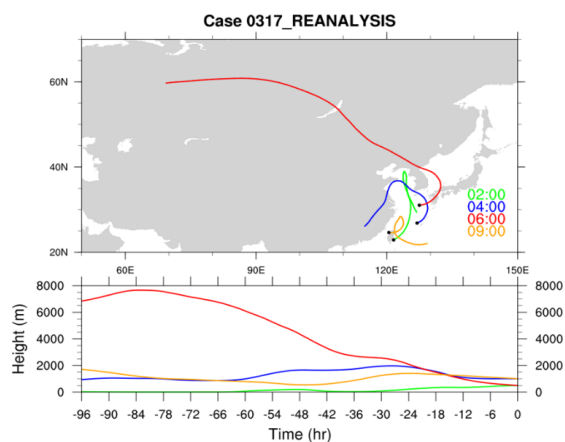
1032

1033

1034

1035

1036

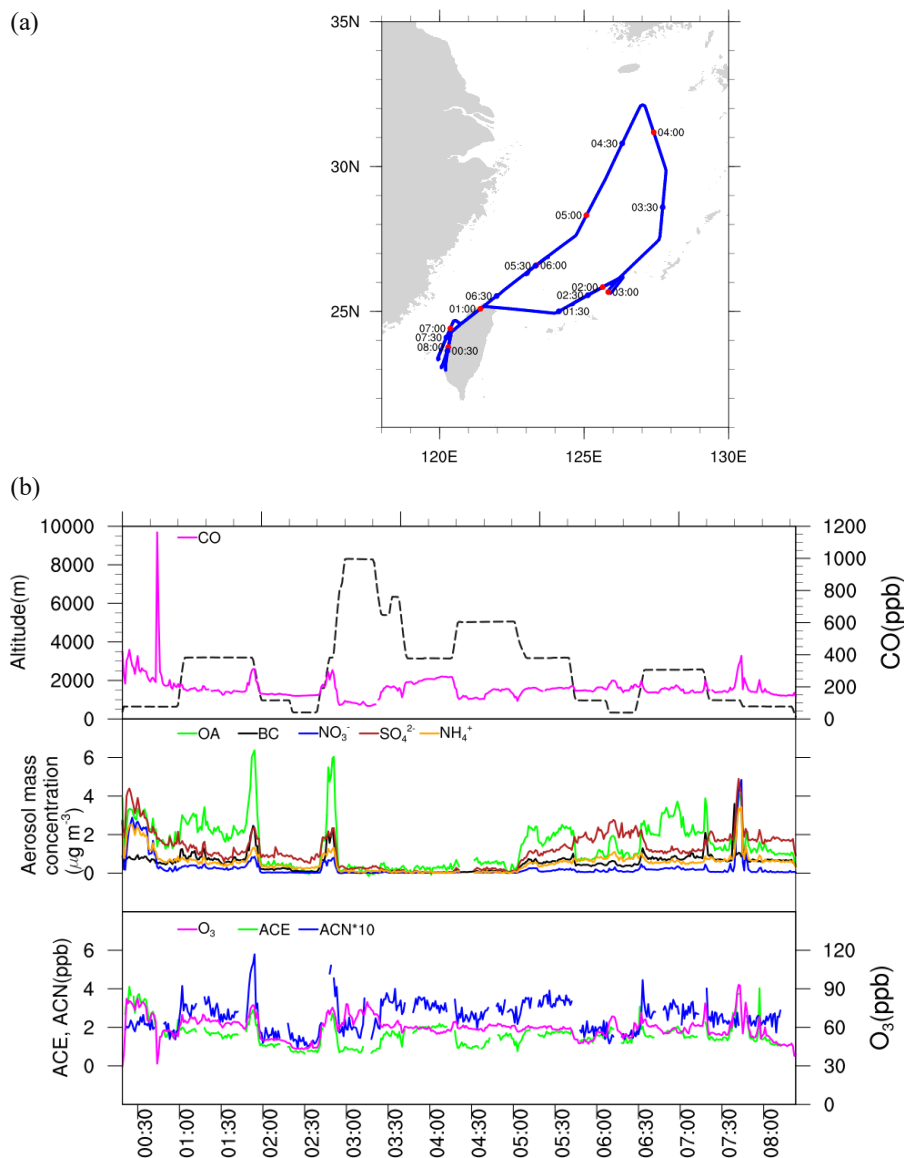


1037 Figure 5 c-e

1038



1039 (a)  
1040  
1041  
1042  
1043  
1044  
1045  
1046  
1047  
1048  
1049  
1050  
1051 (b)



1052  
1053 Figure 6 (a) The HALO flight and detailed locations on 19 March. (b) Flight altitude  
1054 and 1-min mean of observed concentrations for CO (upper), Organic aerosol (OA), BC  
1055 aerosol (BC),  $\text{SO}_4^{2-}$ ,  $\text{NO}_3^-$ ,  $\text{NH}_4^+$  (middle),  $\text{O}_3$ , acetone (ACE) and Acetonitrile (ACN)  
1056 (bottom) on 19 March 2018. (c) The observed  $\text{SO}_4^{2-}$  mass concentration by HALO  
1057 along with height-latitude variations on 19 March 2018 (d) The observed OA mass  
1058 concentration by HALO along with height-latitude variations on 19 March 2018 (e)  
1059 Result of the HYSPLIT model backward trajectory analysis started at the location of  
1060 the HALO flight path at 02:00, 04:00, 05:00, 07:00 UTC on 19 March 2018.



1061 (c)

1062

1063

1064

1065

1066

1067

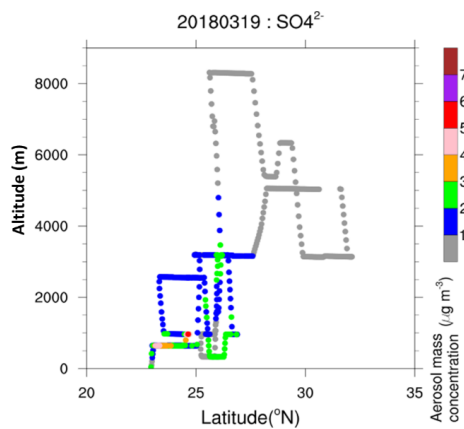
1068

1069

1070

1071

1072



1073 (d)

1074

1075

1076

1077

1078

1079

1080

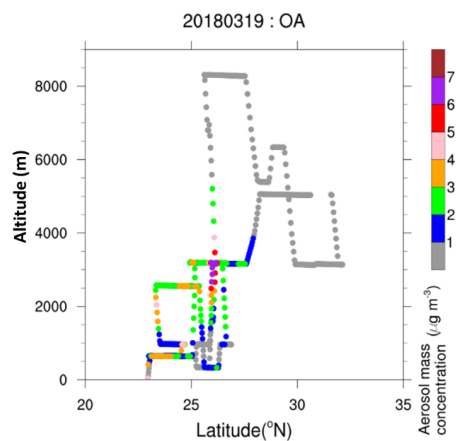
1081

1082

1083

1084

1085



1086 (e)

1087

1088

1089

1090

1091

1092

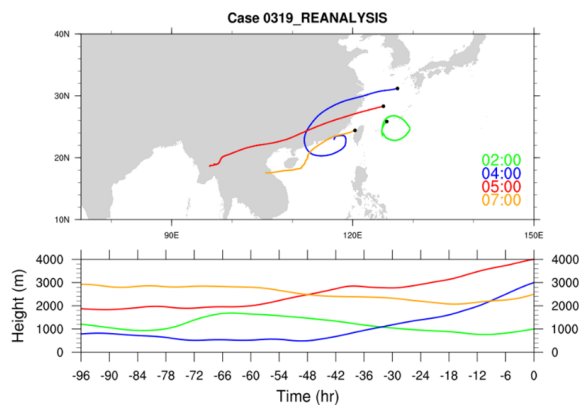
1093

1094

1095

1096

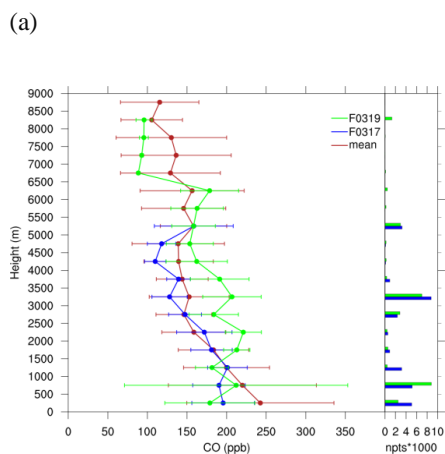
1097



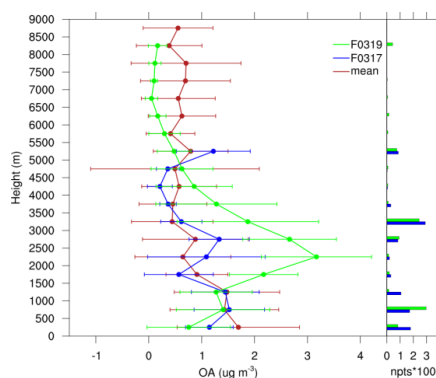
1098 Figure 6 c-e



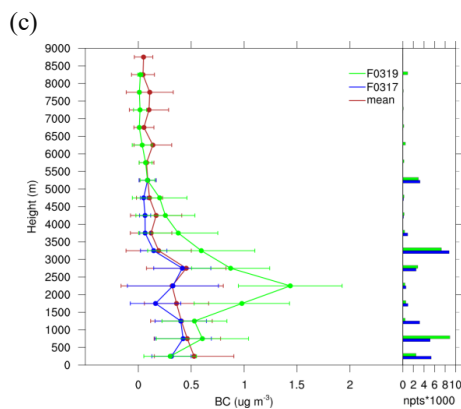
1099  
1100



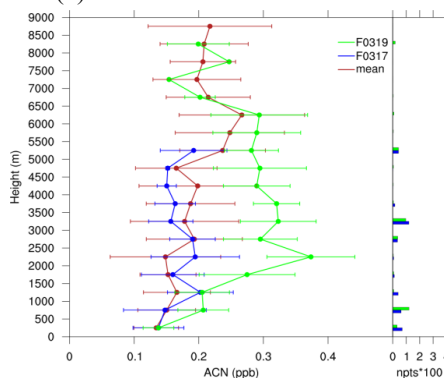
(b)



1101  
1102



(d)

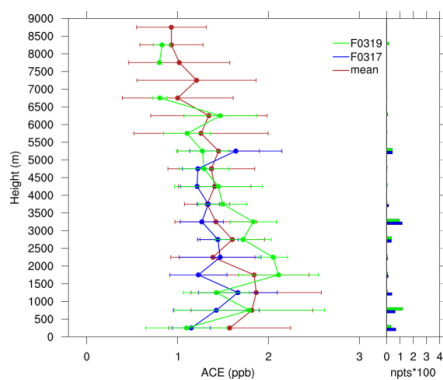


1103  
1104  
1105  
1106  
1107  
1108  
1109  
1110  
1111  
1112  
1113

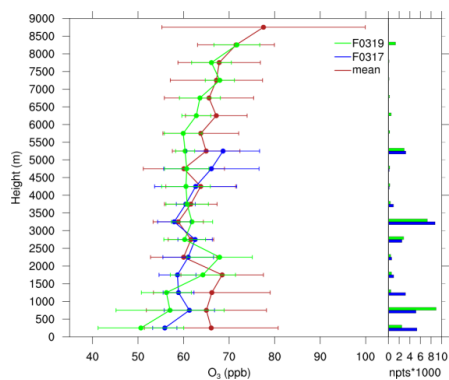
Fig.7 Observed vertical distribution calculated as 1-min mean and 500 m interval with one standard deviation of the concentrations for the mean profiles (red) (including 17, 19, 22, 24, 26, 30 March, and 04 April 2018) and flights on 17 (blue) and 19 (green) March 2018. (a) CO (b) OA (c) BC (d) Acetonitrile (ACN) (e) Acetone (ACE) (f) O<sub>3</sub> (g) J (O<sup>1</sup>D) (h) NO<sub>y</sub>. The number of data points is shown in the right panel.



1114 (e)

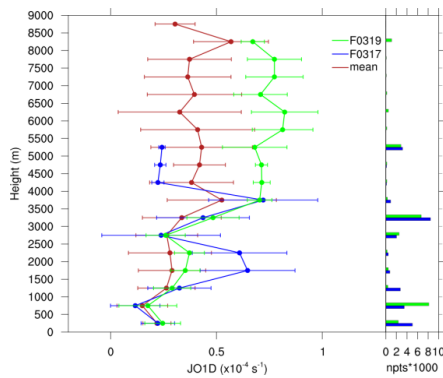


(f)

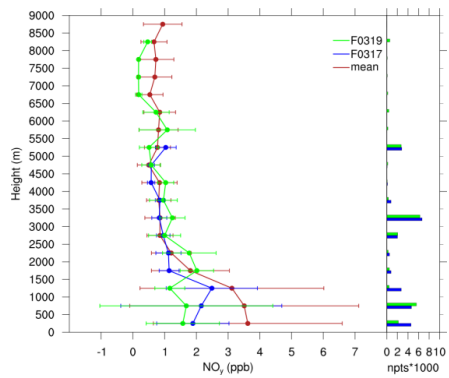


1115

1116 (g)



(h)



1117

1118

1119

1120

1121

1122

1123 Figure 7 continued

1124

1125

1126

1127

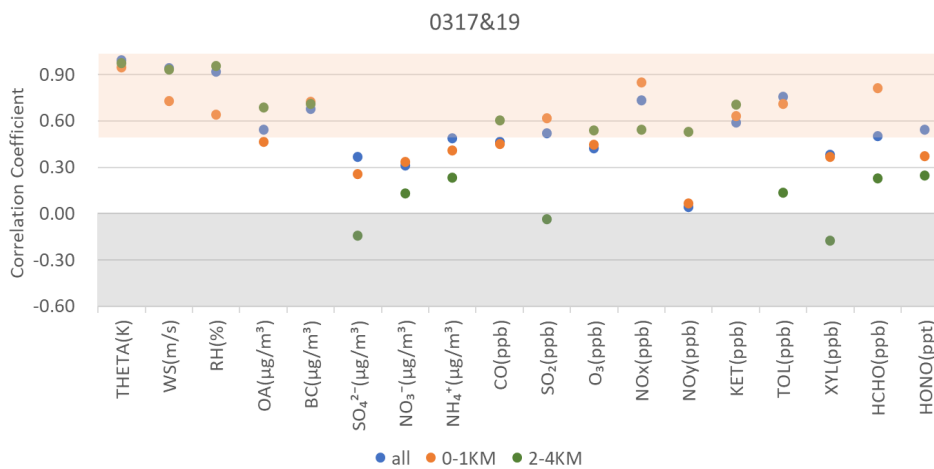
1128

1129

1130



1131



1132

1133

1134 Fig. 8 Correlation Coefficient (R) between observation and simulation along with the  
1135 HALO flights at the elevations 0-1 km, 2-4 km, and the whole track (all) on 17 and 19  
1136 March 2018.

1137

1138

1139

1140

1141

1142

1143

1144

1145

1146

1147

1148

1149

1150

1151

1152

1153

1154

1155

1156



1157 (a)

1158

1159

1160

1161

1162

1163

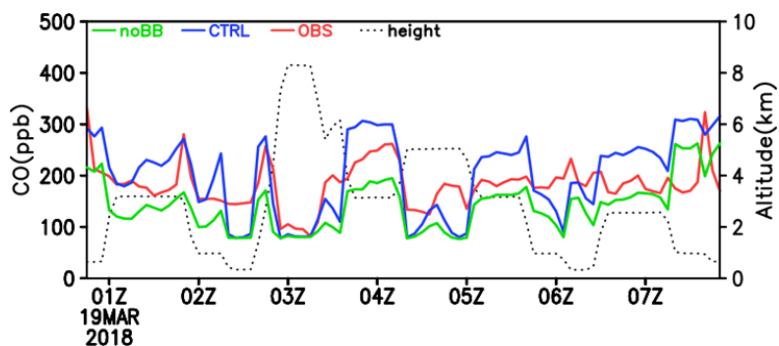
1164

1165

1166

1167

1168



1169 (b)

1170

1171

1172

1173

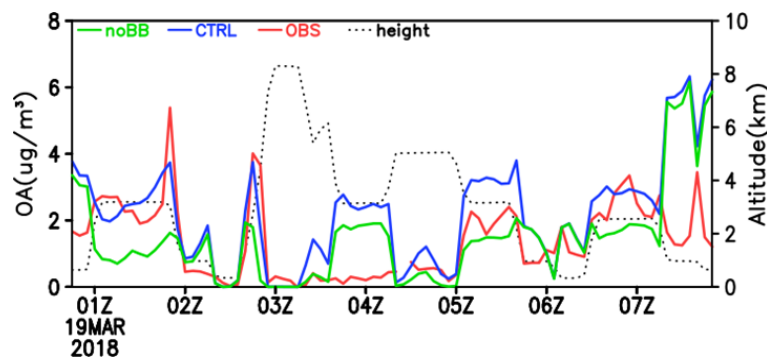
1174

1175

1176

1177

1178



1179 (c)

1180

1181

1182

1183

1184

1185

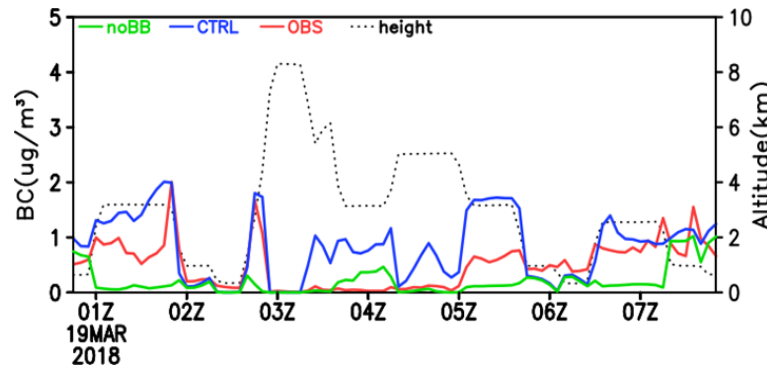
1186

1187

1188

1189

1190

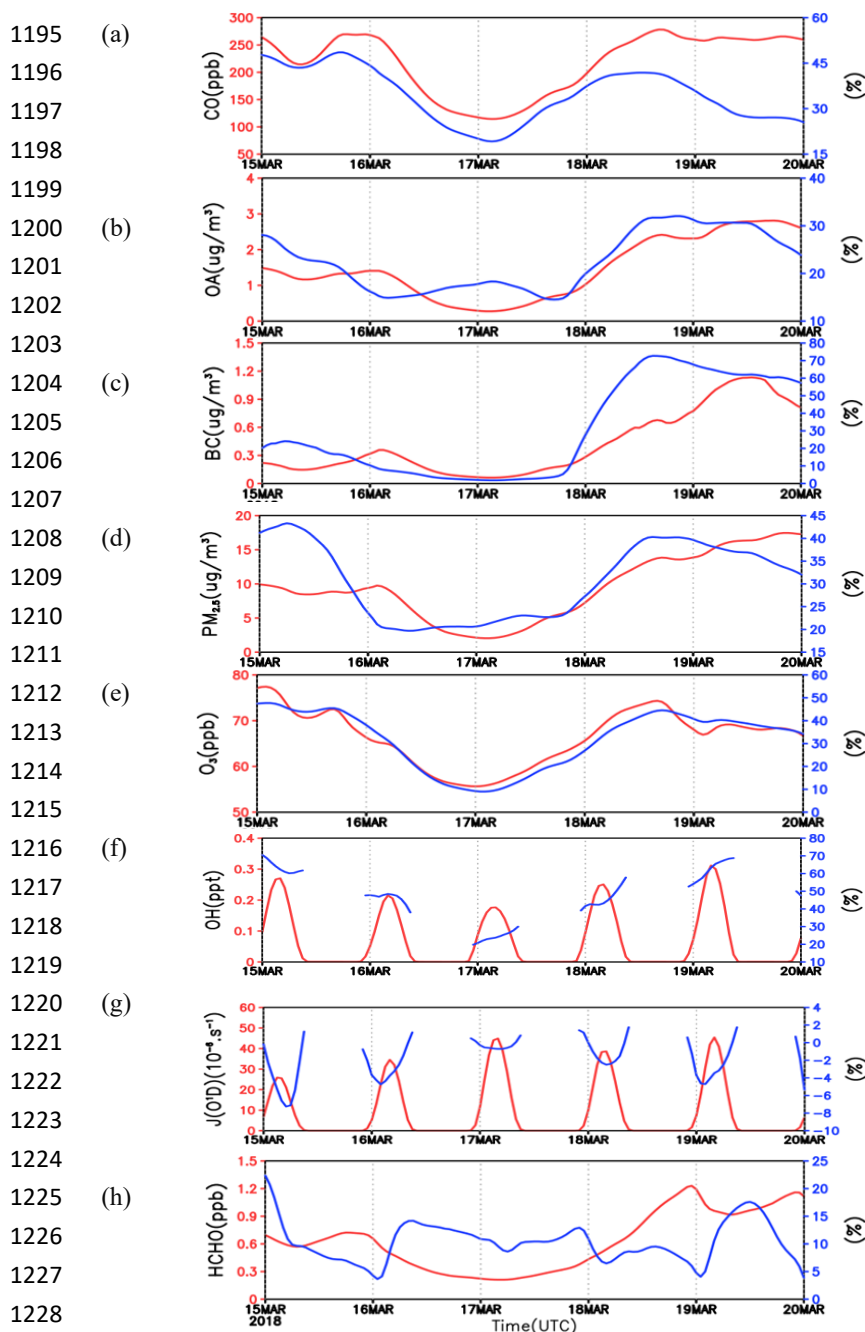


1191 Fig.9 Observed (OBS, red) and simulated concentration with (CTRL, blue) and

1192 without (noBB, green) BB emission along with the flight altitude for (a) CO (ppb) (b)

1193 OA ( $\mu\text{g m}^{-3}$ ) (c) BC ( $\mu\text{g m}^{-3}$ ) on 19 March 2018.

1194



1230 Figure 10 Hourly variation of simulated mean concentration (red) and contributed by  
1231 BB (%), blue) between 2 km and 4 km over the region ECSA in Fig.1a during 15-19  
1232 March 2018. (a) CO (b) OA (c) BC (d) PM<sub>2.5</sub> (e) O<sub>3</sub> (f) OH (g) J(O<sup>1</sup>D), and (h) HCHO



1233

1234

1235

1236 (a)

1237

1238

1239

1240

1241

1242

1243

1244

1245

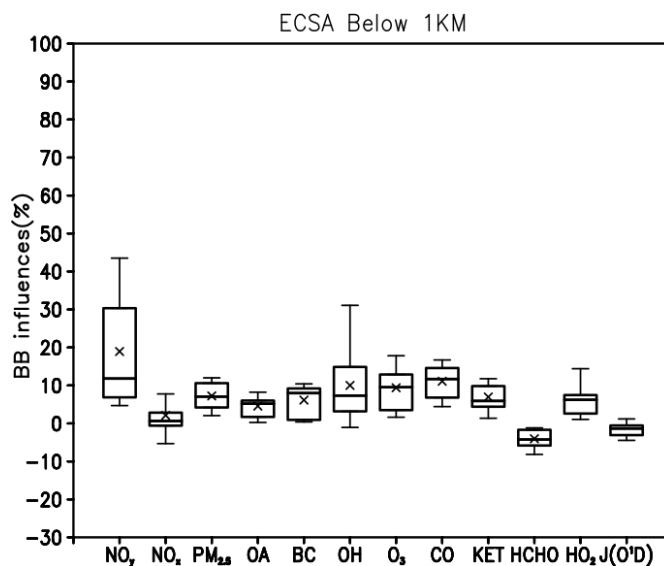
1246

1247

1248

1249

1250



1251 (b)

1252

1253

1254

1255

1256

1257

1258

1259

1260

1261

1262

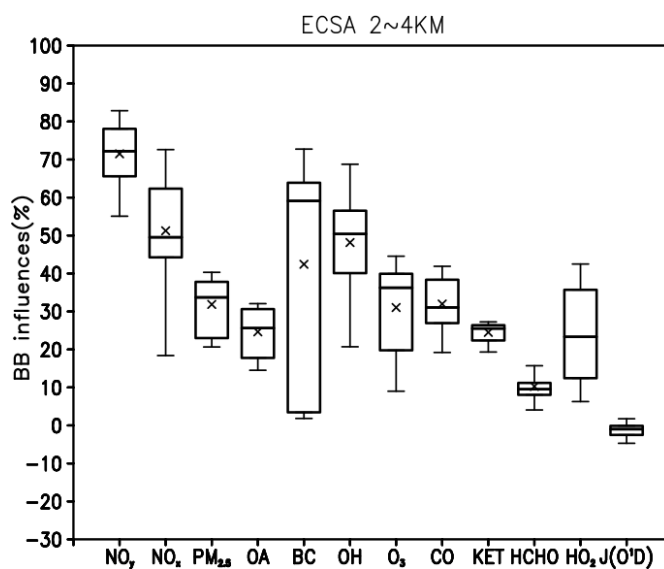
1263

1264

1265

1266

1267



1268

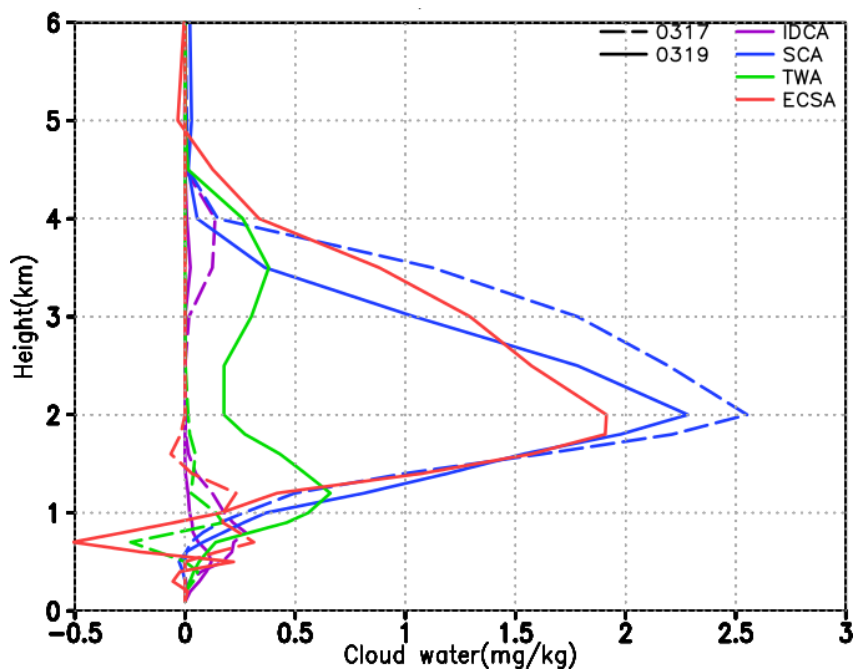
1269

1270

Figure 11 Box plots of simulated BB influences (%) on NO<sub>y</sub>, NO<sub>x</sub>, PM<sub>2.5</sub>, OA, BC, OH, O<sub>3</sub>, CO, KET, HCHO, HO<sub>2</sub>, and J(O<sup>1</sup>D) over the region ECSA in Fig. 1a on 17 and 19 March 2018. (a) below 1 km, (b) between 2 km and 4 km



1271  
1272  
1273  
1274  
1275



1276  
1277  
1278  
1279  
1280  
1281  
1282  
1283  
1284  
1285  
1286  
1287  
1288

Figure 12 Simulated vertical distribution of BB influences on cloud water difference between with and without BB emission on 17 (dash) and 19 (solid) March 2018. Regions include IDCA, SCA, TWA, and ECSA as shown in Figure 1a.